Distinct dystrophin and Wnt/Ror-dependent pathways establish planar-polarized membrane compartments in *C. elegans* muscles

Alice Peysson[1,*], Noura Zariohi[1,*], Marie Gendrel[2], Amandine Chambert-Loir[1], Noémie Frébault[1], Olga Andrini[1], Thomas Boulin[1,#]

[1] Université Claude Bernard Lyon 1, CNRS UMR 5284, INSERM U1314, MeLiS, Lyon 69008, France
[2] Institut de Biologie de l'Ecole Normale Supérieure (IBENS), Ecole Normale Supérieure, CNRS, INSERM, Université Paris Sciences et Lettres Research University, Paris 75005, France
* These authors contributed equally
[#] Lead Contact

Correspondence: thomas.boulin@univ-lyon1.fr

6 Figures, 7 Supplementary Figures

Keywords: Plasma membrane compartmentalization, planar cell polarity, ion channels, Dystrophin-associated protein complex, Wnt signaling, *C. elegans*.

SUMMARY

The plasma membrane of excitable cells is highly structured and molecular scaffolds recruit proteins to specific membrane compartments. Here, we show that potassium channels and proteins belonging to the dystrophin-associated protein complex define multiple types of planar-polarized membrane compartments at the surface of *C. elegans* muscle cells. Surprisingly, conserved planar cell polarity proteins are not required for this process. However, we implicate a Wnt signaling module involving the Wnt ligand EGL-20, the Wnt receptor CAM-1, and the intracellular effector DSH-1/disheveled in the formation of this cell polarity pattern. Moreover, using time-resolved and tissue-specific protein degradation, we demonstrate that muscle cell polarity is a dynamic state, requiring continued presence of DSH-1 throughout post-embryonic life. Our results reveal the intricate, highly reproducible, and entirely unsuspected complexity of the worm's sarcolemma. This novel case of planar cell polarity in a tractable genetic model organism may provide valuable insight into the molecular and cellular mechanisms that regulate cellular organization, allowing specific functions to be compartmentalized within distinct plasma membrane domains.

INTRODUCTION

In neurons and skeletal muscle cells, molecular scaffolds concentrate ion channels in specific membrane sub compartments endowing them with specific functional properties. Distinct cellular mechanisms organize membrane domains such as the axon initial segment, nodes of Ranvier, somato-dendritic compartments and chemical synapses. Large molecular complexes centered around proteins such as ankyrin, PSD-95 or dystrophin organize membrane domains and physically anchor ion channels[1–4]. In addition to controlling their spatial distribution, it is essential that the proper number of ion channels are targeted to these compartments[5]. In epithelial cells, cortical membrane domains are organized by specialized planar cell polarity (PCP) signaling pathways[6]. These PCP cascades integrate extracellular directional cues provided by Wnt ligand gradients, with cell-cell contact based information exchange via membrane-bound protein complexes. This elaborate process allows distinct proteins to be localized asymmetrically within the cell, creating repetitive planar-polarized cellular structures within large cell layers.

The musculature of *Caenorhabditis elegans* is organized into two ventral and two dorsal quadrants that run along the length of the body. Each quadrant is composed of two bands of successive muscle cells[7]. Body wall muscles are diamond-shaped cells when observed in a dorso-ventral view (Figure 1A). They project membrane extensions, called "muscle arms", towards the neurites of presynaptic motoneurons to form post-synaptic domains that concentrate ligand-gated ion channels at chemical synapses. The molecular mechanisms that underlie the construction of these membrane nanodomains have been extensively characterized [8]. In comparison, little is known about how membrane proteins are triaged to other parts of the muscle cell. Muscle cells and sarcomeres are attached to the epidermis via a network of integrin-containing adhesive complexes that cover the outer surface of muscle cells. In addition to integrins, the Dystrophin-Associated Protein Complex (DAPC) physically connects the intracellular actin cytoskeleton to the extracellular matrix along the muscle sarcolemma[7] and have been shown to anchor the BK potassium channel SLO-1[9,10].

Recent transcriptomic analyses have revealed that a surprisingly large number of ion channels genes are co-expressed in *C. elegans* muscle cells raising interesting questions

relating to their temporal dynamics, their subcellular distribution, possible heteromeric assemblies, and individual functions[11–18]. Yet, whether and how these different channels could be addressed to different parts of the muscle cell, or even organized in different submembrane compartments has rarely been addressed.

In this study, we reveal the highly structured organization of the plasma membrane of *C. elegans* body wall muscle cells. By investigating the subcellular localization of ion channels and members of the dystrophin-associated protein complex (DAPC), we show that different proteins partition to distinctive, highly-reproducible, asymmetric membrane compartments. In particular, we found that the potassium channels TWK-28, TWK-24, and SLO-1 occupy distinct, but partially overlapping, polarized compartments at the tip, the center and the posterior part of each muscle cell, respectively. In addition, diffraction-limited microscopy analyses suggest that DAPCs with different compositions exist within a cell, highlighting an additional not previously recognized level of molecular complexity and heterogeneity. Using a forward genetic screening approach, we show that surface expression of TWK-28 is dependent on the dystrophin complex, likely via direct recruitment, but that the dystrophin complex itself is not required for TWK-28's polarized targeting. The asymmetrical distribution of ion channels and DAPC proteins at the cellular and tissue scale is highly reminiscent of canonical planar cell polarity (PCP) patterns. Intriguingly, conserved PCP genes are not involved in this process. However, we found that disheveled/DSH-1, the Wnt receptor Ror/CAM-1, and the Wnt ligand/EGL-20 are required for the asymmetric localization of ion channels and DAPC proteins along the anteroposterior axis of muscle cells. Finally, we show that disheveled is (1) continuously required to maintain cellular polarity, and (2) that post-embryonic expression can restore defective cell polarity, demonstrating that muscle polarity is a dynamic state. Taken together, these results highlight the remarkably complex organization of the worm's sarcolemma. The asymmetric membrane compartments defined by potassium channels and DAPC proteins, repeated in each muscle cell along the length of the animal, constitute the first examples of canonical planar cell polarity patterns in *C. elegans*.

RESULTS

Ion channel localization reveals a remarkably complex and planar-polarized organization of the muscle sarcolemma

Potassium-selective channels are the largest family of ion channels in the *C. elegans* genome. Transcriptomic data indicate that up to 21 distinct potassium channel subunits are co-expressed in body wall muscle cells[11,17]. Yet, little is known about the subcellular localization of most of these channels. To address this question, we used two previously published reporter strains (TWK-18[15]; SLO-1[16]) and engineered knockin lines for six two-pore domain (K2P) channels (TWK-8, TWK-12, TWK-24, TWK-28, TWK-42, TWK-43) using CRISPR/*Cas9*-based gene editing.

Careful analysis of these fluorescent reporters revealed a remarkable diversity of situations. While TWK-8 was present throughout the cell surface (Figure 2F), TWK-12 and TWK-43 were only visible in muscle arms and on the lateral sides of body wall muscle cells, but not on the outer surface that faces the hypodermis (Figure S1A). Conversely, TWK-18 and TWK-42 showed distinct distribution patterns on the outer face of each muscle cell, which were either broad (TWK-18) or punctate (TWK-42) (Figure 2F).

The localization of SLO-1, TWK-24 and TWK-28 were the most striking (Figures 1A and 1B). Indeed, TWK-28 was concentrated at the anterior tip of each muscle cell, in a singular comet-like pattern. Conversely, SLO-1 channels were only present in the posterior part of each

muscle cell, forming a regularly-spaced punctate pattern. Finally, while TWK-24 channels appeared to be broadly distributed at first glance, outlining muscle cells revealed that TWK-24 was in fact absent from their extremities and enriched in the central portion of the cell.

Given that SLO-1, TWK-24, and TWK-28 domains partially overlap at the scale of a muscle cell, we wondered whether they were also colocalized in membrane nanodomains. By simultaneously labeling the three channels and using image segmentation, we observed that individual ion channel clusters were clearly separable even using diffraction-limited confocal microscopy, suggesting that they could be part of distinct protein complexes, even where their distribution patterns overlap at the cellular scale (Figure 1C).

The SLO-1 channel has been shown to physically interact with the integral membrane protein ISLO-1[19]. Therefore, we generated a fluorescent knockin line to assess its subcellular localization. Remarkably, ISLO-1 and SLO-1 did not show identical distribution patterns. While ISLO-1 colocalized with SLO-1 in the posterior part of the cell (Figure 1D), ISLO-1 was also clearly enriched at the anterior tip in a comet-like pattern that coincided perfectly with TWK-28 (Figure 1E). Hence, the distribution pattern of ISLO-1 defines a fourth class of asymmetrical subcellular localization with both anterior and posterior domains, in which ISLO-1 is organized in very different subcellular patterns, i.e., a comet-shaped anterior pattern, and a punctate, regularly-spaced, posterior pattern.

Taken together these observations reveal the remarkably complex molecular makeup of the plasma membrane of *C. elegans* muscle cells. They demonstrate, for the first time, the existence of asymmetric membrane sub-compartments with distinct molecular compositions. Furthermore, as these asymmetric distribution patterns are repeated in each muscle cells all along the length of the worm, they also represent a quintessential case of planar cell polarity at the tissue scale, which has not been observed so far in *C. elegans*.

Dystrophin and dystrophin-associated proteins are required for TWK-28 surface expression

To understand how TWK-28 is targeted to the tip of muscle cells, we performed a forward genetic screen based on the rationale that disruption of factors required to address TWK-28 to the cell surface would suppress the effect of a hyperactivating gain-of-function mutation. We previously demonstrated that the activity of vertebrate and invertebrate two-pore domain potassium channels can be tuned by mutating a single residue in the second transmembrane domain, named TM2.6 [20]. After confirming that this mutation increased TWK-28 activity using heterologous expression in *Xenopus* oocytes (Figure S1B), we used CRISPR/*Cas9* gene editing to build a *twk-28* TM2.6 gain-of-function mutant (*bln485*, TWK-28 L210T). These mutants displayed strongly reduced locomotion, as expected for a gain-of-function mutation that decreases the excitability of muscle cells (Figure S1C).

After screening approx. 15.000 mutagenized haploid genomes, we obtained 182 independent suppressor lines that had regained near wild-type mobility. Among these, 102 were extragenic revertants based on genetic segregation, i.e., mutants that did not alter the *twk-28* gene sequence. Using whole genome resequencing, we analyzed 25 of these mutants and found that 14 were loss-of-function alleles of *dys-1,* the *C. elegans* ortholog of dystrophin, and that one was an allele of *islo-1* (Figure S1D).

To measure their impact on TWK-28 surface expression, we combined *dys-1* and *islo-1* mutants with the fluorescently-labeled TWK-28 reporter (Figures 2A and 2B). We observed a drastic change in *dys-1(bln582)* and *islo-1(bln549)* mutants as the TWK-28 fluorescence was reduced by 74% and 70% relative to wild type, respectively. Interestingly, *dys-1(bln582)* harbors an early stop codon at W110. This mutation affects only the longest dystrophin isoform

that contains both calponin-homology actin-binding domains. To verify whether the remaining TWK-28 fluorescence could be due to residual activity of shorter dystrophin isoforms, we generated *syb2174*, a molecular null allele that deletes the entire 31 kb-long *dys-1* genomic locus. This allele showed the same effect as *bln582*, arguing that the W110Stop mutation is a functional null allele for TWK-28 localization (Figures 2A).

In addition to dystrophin, *C. elegans* muscle express the orthologs of the dystrophin-associated proteins dystrobrevin (*dyb-1*), syntrophin (*stn-1*, *stn-2*), and sarcoglycan/Sgc (*sgca-1*, *sgcb-1*, *sgn-1*). To determine the contribution of these proteins to the surface expression of TWK-28, we first tested sarcoglycan mutants. Loss of individual sarcoglycans or of three Sgc genes at once did not significantly modify TWK-28 fluorescence levels (Figures S1E and S1F). Next, we measured the impact of *dyb-1*, *stn-1,* and *stn-2* mutants (Figures 2B and 2D). *dyb-1(cx36), stn-1(ok292)* and *stn-2(ok2417)* each significantly reduced TWK-28 fluorescence, by approx. 55%, 37%, and 76%, respectively, suggesting a predominant requirement of STN-2. In all cases, residual TWK-28 channels were still restricted to the anterior tip of muscle cells, indicating that targeting of TWK-28 to the comet-like domain is not solely dependent on DAPC proteins.

To assess whether the DAPC was more broadly required for the localization of muscle-expressed K2P channels, we combined four fluorescent knockin lines with a *dys-1* loss-of-function allele. We observed no obvious impact for any of these channels, whether they were uniformly distributed (TWK-8, TWK-18, TWK-42), or asymmetrically localized (TWK-24) (Figure 2F).

Taken together, these results suggested a model in which TWK-28 could be stabilized at the sarcolemma via interactions with the DAPC, as is the case for voltage-gated sodium channels and inwardly-rectifying potassium channels in vertebrate cardiomyocytes [3,4]. Indeed, a short amino acid sequence in the cytoplasmic C-terminus of Nav1.5 and Kir4.1 is recognized by the PDZ domain of syntrophin, which itself binds to dystrophin and thus stabilizes these ion channels at the plasma membrane. Using *in silico* prediction algorithms [21], we identified a putative PDZ-binding sequence in the carboxy-terminus of TWK-28 (Figure 2C). After inserting a premature stop codon that removed these amino acids by gene editing (Figure 2C) in the context of the TWK-28 fluorescent reporter strain, we observed a dramatic reduction in the number of TWK-28 channels (approx. 80%) at the cell surface, similar to *dys-1* and *stn-2* mutants (Figures 2D and 2E). Combining this truncated TWK-28 channel with a molecular null allele of *dys-1* did not further reduce TWK-28-associated fluorescence (Figure 2E), which is consistent with a model in which TWK-28 is directly recognized by syntrophins and stabilized at the plasma membrane by the dystrophin-associated protein complex.

TWK-28 dynamics following post-embryonic DYS-1 degradation and recovery

To examine the dynamics of the relationship between TWK-28 and the DAPC, we developed a temporally-controlled dystrophin degradation strategy using the auxin-inducible degron (AID) system[22]. To monitor DYS-1 levels and subcellular localization, we associated an mNeonGreen coding sequence with the AID degron sequence. This knockin line was fully functional as we did not observe *dys-1* loss-of-function phenotypes (e.g., exaggerated head bending, reduction in TWK-28 surface expression).

Confocal imaging revealed a broad distribution of DYS-1 on the outer face of muscle cells, facing the epidermis (Figure 2H). Consistent with the model that TWK-28 is recruited to the DAPC, DYS-1 and TWK-28 were well colocalized in the anterior tip of each muscle cell (Figure 2I). Hence, DYS-1 is also enriched at the tip of muscle cells, but also distributed more broadly throughout the sarcolemma.

We first tested whether DYS-1 could be degraded by observing the offspring of hermaphrodites grown on auxin (Figures 2G and 2H). Although a very small fraction of the dystrophin-associated fluorescence remained detectable, mNeonGreen fluorescence was drastically diminished in these auxin-treated worms (Figure 2H and 2I). Consistently, worms exposed to auxin throughout their life displayed the exaggerated head-bending phenotype observed in dystrophin null mutants, confirming effective dystrophin degradation. Moreover, the impact of DYS-1 degradation was comparable to *dys-1* null mutants (Figure 2A), since TWK-28 fluorescence was reduced by 73% relative to untreated animals (Figures 2I and 2K).

Using this assay, we could analyze dystrophin dynamics by monitoring fluorescence recovery over 24 hours, starting at the L4 larval stage (Figure 2G). After removing animal from auxin-supplemented media, we observed a partial restoration of DYS-1-mNeonGreen fluorescence throughout the muscle cell and at the anterior tip. TWK-28 fluorescence also recovered notably over the 24-hour time period, but did not reach wild-type levels (Figures 2J, 2K). However, TWK-28 puncta remained closely associated with DYS-1, in line with a direct association of TWK-28 with the DAPC. Interestingly, the overall distribution of TWK-28 and DYS-1 in the comet-like domain was qualitatively different after recovery. It appeared broader and more dispersed than in wild type, which maintained a more condensed pattern (Figure 2J). These data indicate that functional dystrophin complexes can be reassembled post-embryonically, and that TWK-28 requires continuous dystrophin presence to be maintained at the cell surface.

Dystrophin-associated proteins localize to asymmetric membrane compartments

To further characterize the subcellular distribution of dystrophin and dystrophin-associated proteins, we used CRISPR/*Cas9* gene editing to label all members of the worm's DAPC complex[23].

In vertebrates, dystroglycan is a central component of the DAPC, linking the extracellular matrix to the intracellular cytoskeleton via dystrophin. In *C. elegans*, dystroglycan expression has been reported in different cell types, but surprisingly not in muscle[24]. However, clear muscle expression of *dgn-1*, one of three worm dystroglycans, can be detected by single-cell RNA sequencing approaches[11,17]. Consistently, DGN-1 was clearly detectable in body wall muscles in our knock-in line, and DGN-1 was colocalized with DYS-1 on the outer face of muscle cells (Figure 3A). To more precisely describe DGN-1 distribution, we used the dense body marker, PAT-2/α-integrin, as a cellular landmark [25]. Double labeling showed that both proteins occupy distinct membrane domains. Indeed, DGN-1 was excluded from dense bodies and M lines occupied by PAT-2 (Figures 3B, 3C and 3D), even using diffraction-limited light microscopy. These observations demonstrate that dystrophin and dystroglycan are present throughout the sarcolemma of worm muscle cells, and that the DAPC occupies specific membrane nanodomains, juxtaposed to integrin-containing attachment sites.

Sarcoglycans/Sgc are the other major integral membrane component of the DAPC. The Sgc complex is composed of several sarcoglycan subunits (α, β, γ, δ) in skeletal and cardiac muscles [26]. The *C. elegans* genome encodes three sarcoglycans, *sgca-1*, *sgcb-1*, and *sgn-1*, which are orthologs of α-sarcoglycan, β-sarcoglycan, and δ/γ-sarcoglycan, respectively[23]. According to previous reports[19] and transcriptomic data[11], the three sarcoglycan genes are expressed in worm muscles. Using knockin lines, we confirmed their muscular expression and found that sarcoglycans are strictly co-localized (Figures S2A and S2B). In vertebrates, assembly of individual subunits into an oligomeric protein complex is necessary for trafficking to the plasma membrane of muscle cells. Loss of individual subunits strongly decreases sarcoglycan complex formation and membrane targeting[26]. We tested the interdependence of

worm Sgc *in vivo* and found that loss of individual sarcoglycan subunits also strongly disrupted the surface localization of the other two subunits in *C. elegans* (Figure S2C). Moreover, sarcoglycan surface expression was profoundly altered by removing dystrobrevin and dystrophin, either individually or together (Figure S2D). In *dyb-1* mutants, SGCB-1 surface expression was partly reduced in the anterior domain and essentially undetectable in the posterior punctate domain. In *dys-1* mutants, we found a stronger reduction of SGCB-1 and an overall modification of the structure of the anterior domain, rendering it more diffuse. This pattern was also observed in the double mutant, suggesting a dominant role of DYS-1 over DYB-1 for sarcoglycan localization.

Interestingly, sarcoglycan distribution was visibly different from DYS-1, as it appeared more confined (Figure 3E), and strongly resembled ISLO-1 (Figures 1D and 1E). Indeed, sarcoglycans are also found at the anterior tip of the muscle cell in a comet-like pattern, and cluster into a linear pattern of regularly-spaced punctate microdomains in the posterior part of the cell. These two opposite domains are separated by a small region that appears to be mostly devoid of sarcoglycan (Figure 3F). By comparing Sgc and PAT-2 localization, we could observe that, similarly to dystroglycans, sarcoglycans occupy membrane domains that are clearly juxtaposed to integrin complexes (Figure 3F).

Consistently, by comparing DGN-1 and Sgc distributions, we could observe partial colocalization, in particular in the anterior tip of muscles cells, but also in the posterior domain (Figure 3G). In the anterior domain, sarcoglycans mostly co-localized with DGN-1 using diffraction-limited microscopy. However, some DGN-1 puncta were devoid of sarcoglycan, and vice-versa, suggesting a heterogeneous organization of dystroglycan- and sarcoglycan-containing molecular complexes within the sarcolemma (Figure 3G, *anterior domain*). In the posterior part of the cell, the clearly distinguishable sarcoglycan nanodomains co-localized with puncta that were enriched in DGN-1, as compared with the remaining DGN-1 signal. Therefore, these distinct membrane distribution patterns suggest a molecular heterogeneity within the dystrophin-associated protein complex that further illustrates the complexity of the worm's sarcolemma.

Next, we analyzed the distribution of the dystrobrevin ortholog, DYB-1, and the two worm syntrophins STN-1 and STN-2. By comparing their subcellular distributions with DGN-1 and SGCB-1, we observed find that they display two distinct and clearly recognizable localization patterns (Figures S3 and S4). Indeed, STN-2 was broadly expressed and colocalized precisely with DGN-1, while STN-1 and DYB-1 reproduced the more confined distribution pattern of sarcoglycans. Direct comparison of STN-1 and STN-2 confirmed this dichotomy. Finally, by using TWK-28 as a landmark, we confirmed that all DAPC proteins were colocalized with the channel at the anterior tip of muscle cells (Figure S5).

In conclusion, our systematic analysis has revealed that DAPC proteins define multiple membrane subcompartments at the surface of muscle cell, distinct of integrin attachment sites. The clear differences in the distribution of dystroglycans and sarcoglycans provide the first evidence for the existence of DAPCs with different protein compositions.

Dystroglycan localization is dependent on perlecan and intracellular DAPC components

In vertebrates, surface expression of dystroglycan is dependent on interactions with the extracellular matrix protein perlecan[27], and also requires dystrophin[28] and dystrobrevin[29]. First, we tested the role of perlecan/*unc-52* using a viable isoform-specific nonsense allele (*e444*) that eliminates perlecan isoforms expressed in all but the most anterior muscle cells[30]. In these mutant worms, we observed a profound disruption of DGN-1 surface expression (Figure S2E), confirming a conserved genetic link between dystroglycans and perlecans in worms. Next, we

repeated the same analysis with mutants for dystrophin and dystrobrevin (Figure S2F). We observed no obvious modification of the dystroglycan pattern in dystrobrevin/*dyb-1* mutants. However, disruption of *dys-1* using the *syb2174* null allele reduced overall surface expression, disrupted the dense anterior domain, and rendered the DGN-1 pattern more diffuse. Concomitant loss of *dys-1* and *dyb-1* had no additional effect compared to *dys-1* alone.

While the requirement of dystrobrevin may not be conserved in worms, these results confirm the links between dystroglycan/DGN-1 and dystrophin/DYS-1 in *C. elegans* muscle.

Disheveled/DSH-1 controls the asymmetric distribution of membrane proteins

While our forward genetic screen allowed us to demonstrate a requirement of DAPC proteins for the stabilization of TWK-28 channels at the cell surface, it did not reveal the mechanisms that underlie the striking asymmetric distribution of the channels or DAPC proteins within each muscle cell.

Several molecular pathways are known to generate tissue polarity in different cellular contexts. Generally, these involve Wnt ligand/receptor systems and specific proteins belonging to the core planar cell polarity (PCP) pathway[6]. We hypothesized that the polarized organization of TWK-28 could also result from the activity of such tissue polarity pathways, and undertook a candidate gene approach targeting Wnt and PCP genes that are conserved in *C. elegans*[31].

The intracellular effector disheveled is a central player in these molecular cascades as it mediates both canonical and non-canonical Wnt signaling[32]. The *C. elegans* genome encodes three disheveled orthologs: *dsh-1*, *dsh-2,* and *mig-5*. Based on transcriptomic data, *dsh-2* shows little to no detectable expression in muscle cells, contrary to *dsh-1* and *mig-5*[11]. While mutation of *mig-5* had no defect (data not shown), when we combined a *dsh-1* null mutant with the fluorescent TWK-28, SLO-1, and TWK-24 knock-in lines, we observed a striking reorganization of the channels at the muscle surface, leading to a loss of their asymmetric distribution (Figures 4A and 4B). In particular, TWK-28 channels were now found at both extremities of the cell, giving rise to a head-to-tail configuration of anterior and posterior comets in adjacent muscle cells. SLO-1 and TWK-24 distribution was also clearly modified as their domains appeared to shift to a more central position in each cell.

To precisely analyze this redistribution, we measured the position –relative to the length of a given muscle cell– of the boundaries dividing sarcolemmal domains that included or that were devoid of channels (Figure 4C).

First, we found that the anterior border was unchanged in *dsh-1(0)* mutants for each ion channel. TWK-28 channels covered on average 30% of the anterior portion of the cell, while SLO-1 and TWK-24 boundaries were more anterior (23% and 21% respectively) and therefore overlapped slightly with the TWK-28 domain.

In contrast, the posterior borders were markedly displaced. In wild type, we could rarely detect a few clusters of TWK-28 channels at the posterior end of the cell, while in *dsh-1(0)*, TWK-28 channels covered over 25% of it. Thus, anterior and posterior TWK-28 domains were now almost symmetrical. In the case of SLO-1, the posterior boundary that usually extended almost to the end of the cell, now shifted anteriorly, uncovering close to a fourth of the posterior portion of the cell. Conversely, the TWK-24 domain extended more posteriorly in *dsh-1(0)*, now closely matching the distribution of SLO-1 channels. Interestingly, image segmentation of triple-labelled cells revealed that the three channels remained optically-separable even using diffraction-limited microscopy, suggesting that they still partition into physically distinct nano-domains within the sarcolemma (Figure 4D).

Next, we wondered whether the redistribution of TWK-28 channels also affected their surface expression levels. Based on fluorescence quantification of entire muscle cells, we found that the total number of channels was unchanged in *dsh-1* mutants. Indeed, TWK-28 fluorescence was split between anterior and posterior comets, consistent with the respective size of each domain (Figure 4E). These data thus suggest that the number of TWK-28 channels present at the cell surface is limited and finely regulated by mechanisms that are independent of disheveled/*dsh-1*.

Given the requirement of dystrophin for TWK-28 surface expression, we hypothesized that DYS-1 distribution must also be altered in *dsh-1* mutants. Using TWK-28 as a landmark, we could clearly observe that dystrophin was indeed present at both extremities of muscle cells (Figure 4F) in a *dsh-1* null mutant. The sarcoglycan SGCB-1 similarly adopted a symmetrical distribution pattern, further strengthening the notion that *dsh-1* plays a major role to ensure muscle cell asymmetry (Figure 4G).

Finally, to further investigate the interplay between processes that control TWK-28 surface distribution via dystrophin and DSH-1, we used the TWK-28 mutant lacking the C-terminal PDZ-binding sequence (Figure 2C), as it decouples TWK-28 from the DAPC. Indeed, in this context, we could still detect an accumulation of TWK-28 channels at the posterior end in *dsh-1* null mutants (Figure 4H), arguing that TWK-28 channel are addressed to the extremities of muscles cells independently of their interaction with the DAPC, and that the DAPC likely serves to stabilize TWK-28 at the surface in a second step.

Taken together, these data support a model in which DSH-1 ensures that dystrophin and TWK-28 are not addressed or maintained at the posterior end of muscle cells, while the DAPC, subsequently and independently, stabilizes TWK-28 channels at the cell surface. The process that addresses DYS-1, SGCB-1, and TWK-28 to the extremities of muscle cells remains to be determined.

The DIX domain of DSH-1 is dispensable for TWK-28 asymmetry

Disheveled proteins comprise three conserved functional domains: DIX, PDZ and DEP (Figure 5A). Generally, DIX and PDZ domains are required for canonical Wnt β-catenin signaling, while PDZ and DEP domains function in PCP signaling[32]. To investigate which pathways may act downstream of DSH-1 in muscle cells, we expressed a series of protein truncations in body wall muscle cells and monitored the rescue of TWK-28 localization in a *dsh-1* mutant background (Figure 5B). First, we verified that a *dsh-1a* cDNA was sufficient to restore TWK-28 localization (i.e., panel "+ *Pmyo-3::dsh-1a*"). Next, we expressed truncated *dsh-1a* cDNAs lacking each domain using the same muscle-specific promoter, and found that only the cDNA lacking the DIX domain restored TWK-28 localization in a *dsh-1* null mutant.

These results indicate that PDZ and DEP domains are indispensable for TWK-28 targeting, pointing to an involvement of PCP-type signaling downstream of DSH-1. They also show that DSH-1 likely does not engage canonical β-catenin-dependent signaling in this context, a conclusion that was consistent with a lack of TWK-28 redistribution in *bar-1*/β-catenin mutant worms (Figure 5C).

Sarcolemmal asymmetry requires Wnt/Ror but not PCP proteins

Given the results of our DSH-1 structure-function analysis, we proceeded to test the possible involvement of genes belonging to the two planar polarity pathways: the core PCP proteins, VANG-1/Stan, FMI-1/Flamingo, and PRKL-1/Prickle, and the global proteins, CDH-1/Dachsous and CDH-3/CDH-4/Fat. Surprisingly, none of these genes were required for planar-polarized TWK-28 localization (Figure 5C).

Given these results, we investigated the involvement of Wnt-dependent pathways. First, we tested a viable *mig-14*/Wntless hypomorphic mutant that reduces the secretion of Wnt ligands and found that it led to a loss of TWK-28 polarity (Figure 5D). Next, we analyzed viable mutants for four Wnt ligands and found that *egl-20* altered the localization of TWK-28 (Figures 5D). Finally, we tested five transmembrane proteins that bind Wnt ligands: the Wnt receptors LIN-17, MIG-1, CFZ-2, LIN-18/Ryk and the receptor tyrosine kinase CAM-1/ROR. *lin-17* and *lin-18*, alone, and *mig-1 cfz-2* double mutants had no effect (Figures S6A and S6B), while the reference allele of *cam-1* phenocopied *egl-20* mutants (Figures 5D and 5E). To confirm these results, we generated an early stop codon at position Pro21 in EGL-20 using CRISPR/*Cas9* gene editing (Figure S6C), and analyzed three additional *cam-1* alleles (*ak37*, *cw82*, *ks52*) (Figures 5E and 5F). These four additional mutant alleles all showed phenotypes identical to the reference alleles.

Observing the impact of these gene mutations in more detail along the entire length of the animal provided some additional information about the molecular actors upstream of disheveled. Indeed, *mig-14*, *egl-20*, and *cam-1* mutants only affected the distribution of TWK-28 in muscle cells that were posterior or close to the vulva (anteriorly), while *dsh-1* mutation also affected muscle cells situated more anteriorly (Figure 5D).

This spatially-restricted effect is consistent with the known range of the EGL-20 gradient that is formed by secretion from cells in the tail of the worm, extending to the midbody[33,34]. Furthermore, *cam-1* mutation also did not affect cells anterior to the vulva, which could indicate that a different Wnt receptor/Wnt ligand combination is acting in these cells, or that redundant pathways control muscle polarity in the anterior half of the worm.

Subcellular distribution of DSH-1 in body wall muscle cells

To gain further insight into how DSH-1 controls muscle membrane asymmetry, we analyzed the subcellular distribution of DSH-1 in three translational knockin lines in which the mNeonGreen coding sequence was inserted at the N- and C-terminus, and between the DIX and PDZ domains[25] of DSH-1.

To ensure that these mNeonGreen-tagged DSH-1 chimeras remained functional, we used TWK-28 localization as a proxy for DSH-1 function. Interestingly, although the three lines showed similar fluorescence patterns, only the N- and C-terminal insertions were fully functional, while TWK-28 channels were mislocalized in the intra-molecular insertion line (data not shown).

Using the C-terminally tagged *dsh-1* alleles (*bab365*), we analyzed the distribution of DSH-1 proteins within muscle cells. Remarkably, DSH-1 was enriched in the posterior third of body wall muscle cells (Figures 6A and 6B), clearly distinct of TWK-28's anterior localization (Figures 6C). This pattern was lost in *cam-1* and *egl-20* mutants (Figures S7A). Interestingly, while *egl-20* disrupted DSH-1 localization only in muscle cells that were posterior to the vulva—consistent with the EGL-20 gradient—, loss of *cam-1* affected DSH-1 distribution all along the body. Yet, TWK-28 asymmetry was not affected in *cam-1* mutants anterior to the vulva.

DSH-1 is continuously required to establish and maintain muscle membrane polarity

Next, we wondered whether muscle polarity was a fixed or a dynamic state, i.e., whether DSH-1 was only required to establish muscle polarity, or also to maintain it throughout the life to the worm. Therefore, in addition to mNeonGreen, we inserted the AID degron sequence into our DSH-1-mNeonGreen knockin line to be able to manipulate DSH-1 protein levels and study its temporal window of action.

First, to validate this approach, we exposed fourth stage (L4) larvae to auxin and –three days later– analyzed their F1 progeny at the L4 stage. Using a transgenic line expressing TIR1 ubiquitously, we could observe a robust degradation of DSH-1-mNeonGreen and a clear redistribution of TWK-28 channels into a symmetrical localization pattern, phenocopying the *dsh-1(0)* mutant (Figure S7B).

Next, to determine the appropriate time window for DSH-1 degradation, we observed the localization pattern of TWK-28 during the first three larval stages, in wild-type and *dsh-1(0)* worms (Figure 6D). While muscle polarity was fully established at the second (L2) and third (L3) larval stages, we observed both polarized and non-polarized cells in freshly-hatched (L1) larvae. This suggests that TWK-28 polarity is mostly established during embryogenesis, and that it may derive from an initially non-polarized state.

We also noted that the shape of TWK-28-containing comets changed progressively. Only a small number of fluorescent clusters were observed in the L1. In the L2 and L3 stages, the number of clusters increased, accompanied by a widening of the comet over time. Loss of *dsh-1* disrupted muscle polarity at all larval stages (Figure 6D).

To determine whether *dsh-1* was required to maintain muscle polarity once it was established, we started degrading DSH-1-mNeonGreen at the L3 larval stage and observed these worms 72 hours later. This protocol led to a clear loss of TWK-28 asymmetry, demonstrating that muscle polarity is a dynamic state, and that DSH-1 is continuously required to maintain it (Figure 6E).

Conversely, we asked whether restoring DSH-1 expression post-embryonically could restore muscle polarity starting from a non-polarized state. In this case, we exposed animals to auxin until the L3 stage, and monitored the recovery of DSH-1 levels and muscle polarity over 72 hours (Figure 6F). First, as in our initial experiment with L4 stage animals (Figure S7B), L3 animals exposed to auxin throughout their life also showed a clear loss of muscle polarity and an absence of DSH-1-associated fluorescence. Next, over the course of the 72-hour recovery period (i.e., in the absence of auxin) we could observe a clear restoration of the polarity pattern.

These two complementary experiments directly demonstrate that DSH-1 is required –thorough the life of the animal– to establish and to maintain the polarity of *C. elegans* muscle cells, and that this state is therefore dynamic and could be regulated by extracellular signals that would impact DSH-1 activity.

DISCUSSION

By analyzing the subcellular distribution of potassium channels and proteins linked to the dystrophin-associated protein complex, we reveal here the previously unsuspected compartmentalization and planar-polarized organization of the sarcolemma of *C. elegans* muscle cells. Despite decades of detailed work on the structure of *C. elegans* muscle cells[7], this remarkable case of cellular polarization was entirely unsuspected.

Sarcolemmal asymmetry at the cellular scale

Our initial analysis of single-cell RNAseq data and other published reports had indicated that up to 21 potassium channel subunits could be co-expressed in body wall muscle cells. Apart from the extensive work regarding the precise targeting of ligand-gated ion channels to the ends of muscle arms[8], whether ion channels could be differentially targeted to different parts of the sarcolemma has been rarely addressed specifically. By revealing the distinct subcellular localization patterns of different potassium channels, we have demonstrated that clear

differences exist in the molecular composition of the muscle's plasma membrane. For instance, while TWK-8 and TWK-18 channels are found throughout the sarcolemma, TWK-12 and TWK-43 channels are only targeted to the basolateral membrane and muscle arms. Conversely, TWK-28 and TWK-42 channels are only found on the outer side of the muscle cell, facing the epidermis, and not on the lateral membrane or muscle arms. Importantly, the comparison of TWK-28, TWK-24 and SLO-1 channels shows that even when channels are located in the same region of the sarcolemma (i.e., the outer face of the cell), they can occupy distinct –yet partially overlapping– regions along the antero-posterior axis. And even when they are present in overlapping regions, we could show that ion channels remain confined to distinct nanodomains. The high reproducibility of these patterns between different individuals and within muscle cells of a single animal imply that specific molecular and cellular mechanisms must target individual channels to their respective domains, likely endowing them with distinct electrophysiological properties.

Another remarkable observation is the difference in organization of TWK-28, ISLO-1 and SLO-1. ISLO-1 interacts with SLO-1 and the syntrophin STN-1, allowing the recruitment of the BK potassium channel to the DAPC, and mutations of *islo-1* and *dys-1* disrupt surface expression of SLO-1 in muscle cells[9]. However, we have shown here that ISLO-1 and SLO-1 localization patterns are not identical since ISLO-1 is also present in the comet-like domain at the anterior tip of each muscle cell. Similarly, we have found that *islo-1, dys-1* and syntrophins are necessary for TWK-28 surface expression, but TWK-28 is nevertheless restricted to the anterior domain. Notably, even when cellular polarity is disrupted by mutations in Wnt/Ror and *dsh-1*, the posteriorly-localized TWK-28 does not reproduce the posterior, punctate, ISLO-1 pattern, but rather mirrors the comet-like distribution seen at the anterior tip in wild-type animals. Therefore, there are likely specific molecular actors that allow the selective recruitment of TWK-28 and SLO-1 to distinct anterior and posterior domains. Forward genetic screens could directly address this question in the future by identifying gene mutations in which TWK-28 or SLO-1 channels are no longer restricted to their anterior or posterior domains, but rather redistributed into an ISLO-1-like pattern.

The dystrophin-associated complex as an organizer of plasma membrane compartments

Detailed analyses of the distribution of DAPC proteins further highlight the complex organization of the muscle membrane. At first glance, DAPC components can be separated into two classes: one class that includes DGN-1, DYS-1 and STN-2, and the other that consists of sarcoglycans, DYB-1 and STN-1. One-to-one colocalization studies however reveal that there is significant overlap between both groups. For example, the posterior sarcoglycan puncta coincide with areas of denser DGN-1 signal, which is surrounded by weaker DGN-1-associated fluorescence. This could be explained by different diffusion kinetics with one predominant population of confined sarcoglycans versus two populations of confined *versus* freely diffusing dystroglycans. Fluorescence recovery or photoconversion approaches could be used in the future to address this question *in vivo*.

Although DAPC proteins are generally thought to be part of the same molecular complex, our observations challenge the notion of a singular DAPC composition. For example, we observed a heterogeneous organization of dystroglycan- and sarcoglycan-containing molecular complexes in the anterior tip of muscle cells where some DGN-1 puncta were devoid of sarcoglycan, and vice-versa. In mammals, while costameric DAPCs are thought to contain all components, the situation is also more complex at the neuromuscular junction where they are all present but not colocalized and not involved in the same functions[35]. It is also interesting

to note the clear separation of DAPC and integrin complexes in worm muscles. Using diffraction-limited microscopy, fluorescent markers could be easily distinguished suggesting that they are situated far from each other, thus refining previous analyses that suggested a close association with dense bodies in the I-band[36]. It thus remains to be determined which molecular partners or scaffolds underpin the highly stereotyped subcellular distribution of DAPC proteins.

To definitively clarify DAPC localization in worm muscles and determine the exact molecular makeup of dystrophin-containing nanodomains, it will be essential to move beyond diffraction-limited microscopy and resort to state-of-the-art super-resolution techniques. The vast increase in resolution afforded by super-resolution light microscopy will clarify the composition of membrane nanodomains and relative distribution of dystrophin and its associated proteins. As shown here, dystrophin and sarcoglycans occupy both overlapping and distinct sub-membrane domains. Yet, even when they appear co-localized using conventional confocal microscopy, they could still occupy distinct nanodomains. Refining their relative location will reveal the heterogeneity within DAPC complexes at the surface of muscle cells. Similarly, the two worm syntrophins, STN-1 and STN-2, have distinct and partially overlapping distribution patterns in muscle cells. We have also found that they contribute differently to the surface expression of the potassium channel TWK-28. Fly and vertebrates also co-express multiple syntrophins with different subcellular localizations and functions[37]. Thus, understanding the interplay between these two worm syntrophins may provide new leads on the mode of action of syntrophins.

Interestingly, recent observations in different cellular contexts have revealed intriguing asymmetric distribution patterns and functions of the DAPC. Indeed, precise *in vivo* studies of dystrophin in mouse models have been greatly improved by the generation of GFP-tagged mouse knockin lines. These models have confirmed the broad distribution of dystrophin along the membrane of muscle fibers[38,39] but also revealed a striking enrichment at the extremities of muscle fibers[40]. Asymmetric localization of dystrophin has also been described in zebrafish muscles[41]. Analysis of a gene trap line that fluorescently labels the endogenous dystrophin protein showed that dystrophin is highly enriched at myosepta –the contact site that separate two somites– forming a repetitive chevron-like structure along the length of the body of the fish. During development, more dystrophin is recruited to this interface, exacerbating the asymmetric organization of dystrophin within growing muscle fibers. In activated rodent muscle stem cells (i.e., satellite cells) dystrophin is located apically in close contact with the extracellular matrix. This polarized distribution of dystrophin regulates the asymmetric division of satellite cells via the recruitment of the serine-threonine kinase Par1b[42]. In drosophila epithelial follicle cells, recent functional studies have shown that the DAPC promotes planar polarization of integrin clusters and participates in the trafficking of ECM components leading to the formation of polarized fibrils[43]. These observations suggest that the DAPC may be at the heart of cellular mechanisms that precisely define subcellular cortical domains allowing specific functions to be compartmentalized within a single cell.

Planar cell polarity at the scale of the muscle tissue

The *C. elegans* body wall muscle tissue is organized in four quadrants that are each composed of two bands of successive muscle cells[7] (Figure 1A). Each muscle quadrant is essentially a single layer of muscle cells that runs along the length of the animal. The asymmetrical distribution of potassium channels and DAPC proteins within each muscle cell therefore translates into a prototypical planar polarity pattern. Most planar cell polarity genes are conserved in the *C. elegans* genome[31]. The role of VANG-1, PRKL-1, and FMI-1 in cell

migration-related processes have been well established. PCP proteins regulate cell intercalation, convergent extension movements, neuronal migration, neurite outgrowth and guidance. However, in contrast to planar cell polarity in fly epithelia, worm PCP proteins act on an individual cell basis rather than via cell-cell contact-dependent polarization processes. They have been mostly found to control asymmetry pathways that instruct antero-posterior polarity and asymmetric cell divisions during embryogenesis and larval stages. They also control the asymmetric divisions of the stem-cell-like epithelial seam cells. Their action in these contexts is transient. In contrast, the planar polarity patterns we have described here remain visible throughout the life of the cell. Consistently, continuous activity of DSH-1 is required to maintain membrane organization and muscle polarity. Indeed, by manipulating DSH-1 levels at different life stages, we could demonstrate that muscle polarity is not a fixed state, established early on in muscle cells. Continuous requirement of DSH-1 argues that it controls a dynamic machinery. It will therefore be essential to identify the molecular targets of DSH-1 in muscle cells, and to identify additional factors required to establish and maintain muscle polarity. Further work will be required to dissect the molecular and cellular signaling pathways that control this novel example of planar cell polarity in the nematode *Caenorhabditis elegans*.

ACKNOWLEDGEMENTS

We thank Hannes Bülow and Jean-Louis Bessereau for critical reading and comments about the manuscript. This work was funded by a grant to T.B. from the European Research Council (ERC Stg 2013, *Kelegans*) and AFM Téléthon (Alliance MyoNeurALP). A.P. was supported by AFM Téléthon and LabEx CORTEX. We thank *Le Centre d'Imagerie Quantitative Lyon-Est* (LyMIC-CIQLE, Lyon, France) imaging facility for support and access to equipment. Some strains were generated by SEGiCel (SFR Santé Lyon Est CNRS UAR 3453, Lyon, France) with funding provided by TEFOR to K. Gieseler. Some strains were provided by the CGC, which is funded by NIH Office of Research Infrastructure Programs (P40 OD010440). Some strains were provided by the National Bioresource Project at the Tokyo Women's Medical University School of Medicine, which is part of the International *C. elegans* Gene Knockout Consortium.

The authors declare no competing financial interests.

MATERIALS & METHODS

RESOURCE AVAILABILITY

Lead Contact

Further information and requests for resources and reagents should be directed to and will be fulfilled by the Lead Contact, Thomas Boulin (thomas.boulin@univ-lyon1.fr).

Materials Availability

Worm strains and plasmids generated in this study are available upon request.

EXPERIMENTAL MODEL AND SUBJECT DETAILS

Strains and genetics

All *C. elegans* strains were originally derived from the wild-type Bristol N2 strain. Worm cultivation, genetic crosses, and manipulation of *C. elegans* were carried out according to standard protocols[44]. All strains were maintained at 20°C on nematode growth medium (NGM) agar plates with *Escherichia coli* OP50 as a food source. Strains and alleles used for this study are listed in Supplementary Table S1 and S2, respectively.

METHOD DETAILS

Molecular biology

Single-strand oligonucleotides, crRNA, and plasmids used in this study are described in Supplementary Table 3, 4, and 5, respectively.

Auxin-induced degradation

Auxin plates were prepared by adding auxin Indole-3-Acetic Acid (Sigma) from a 400 mM stock solution in ethanol into NGM at the final concentration of 1 mM[22]. DYS-1 and DSH-1 degradation was performed using a transgene expressing TIR1 with the ubiquitous promoter *Peft-3*[45]. Protein degradation was monitored *in vivo* based on mNeonGreen fluorescence.

Microscopy imaging and quantification

General methods Freely moving worms were observed on nematode growth media (NGM) plates using an AZ100 macroscope (Nikon) equipped with a Flash 4.0 CMOS camera (Hamamatsu Photonics). For confocal imaging, animals were mounted on 2% dry agarose pads with 2% poly-lysine beads in M9 buffer (3 g KH_2PO_4, 6 g Na_2HPO_4, 5 g NaCl, 0.25 g $MgSO_4 \cdot 7\ H_2O$, and distilled water up to 1 liter). Confocal imaging was performed using an inverted confocal microscope (Olympus IX83) equipped with a confocal scanner unit spinning-disk scan head (Yokogawa) and an EMCDD camera (iXon Ultra 888, Andor) at the Ciqle imaging facility (Centre d'Imagerie Quantitative Lyon-Est, LyMIC-CIQLE, Lyon, France).

TWK-28-mNeonGreen fluorescence intensity quantification Quantification of fluorescent images were performed using ImageJ (version: 2.0.-rc-69/1.53a). Each data point represents one muscle cell and data from at least three independent imaging sessions were pooled for each genotype. Acquisition parameters were the same across genotypes for quantitative analyses. Fluorescence intensity was measured from Figure 2A to 2E) in a region of interest of 30 µm (wide) x 5 µm (high) size, and for Figure 2K in a region of interest of 50 µm (wide) x 5 µm (high) size. To quantify the fluorescence intensity of TWK-28 in figure 4E, we first segmented individual muscle cells using TWK-12::wrmScarlet to outline the muscle membrane. The total fluorescence intensity was corrected by subtracting background fluorescence from the middle of the cell, where TWK-28 was undetectable.

Measurement of TWK-28, TWK-24 and SLO-1 domain boundaries To determine the precise outline of individual muscle cells, we used TWK-12::wrmScarlet for cell membrane segmentation. We then manually measured the length of each cell and the relative position of the TWK-28, TWK-24 and SLO-1 domain boundaries along the antero-posterior axis (Figure 4C).

Electrophysiology and heterologous expression of TWK-28 in *Xenopus laevis* oocytes

Capped mRNAs were synthesized in vitro from linearized expression vectors using the T7 mMessage mMachine kit (Ambion, Austin, TX, USA). Defolliculated *X. laevis* oocytes (Ecocyte Bioscience, Dortmund, Germany) were injected with 50 nL containing 1.8 ng of cRNA. Oocytes were kept at 18°C in ORII Calcium solution containing (in millimolar): 82.5 NaCl, 2 KCl, 1 $MgCl_2$, 0.7 $CaCl_2$, 5 HEPES, gentamicin (25 µg/mL), pH 7.5 (with TRIZMA-Base).
Two-electrode voltage clamp (TEVC) experiments were performed 24 hours after microinjection. Oocytes were mounted in a small home-made recording chamber and continuously superfused with ND96 solution containing (in millimolar): 96 NaCl, 2 KCl, 1.8 $CaCl_2$, 2 $MgCl_2$, 5 HEPES. pH 7.4 was adjusted with Trizma base. Macroscopic currents were recorded using a Warner Instrument OC-725 amplifier, filtered at 10kHz, digitized using a Digidata-1322 (Axon Instrument). For current visualization and stimulation protocol application,

718 we used Axon pClamp 9 software (Molecular Devices, Sunnyvale, CA). Recording electrodes
719 were pulled to 0.2-1.0 MΩ by using a horizontal puller (Sutter Instrument, Model P-97, USA)
720 and filled with 3 M KCl. Currents were recorded in response to a voltage-step protocol
721 consisting of a pre-pulse of -80 mV (80 ms duration) from a holding potential of -60 mV,
722 followed by 10 mV steps (200 ms duration) from -150 mV to +50 mV, and return to a -60 mV
723 holding potential. Current-voltage curves were obtained by plotting the steady-state currents
724 at the end of each voltage step.
725
726 **QUANTIFICATION AND STATISTICAL ANALYSIS**
727 The statistical analysis was performed using the R software package. Normality of sample
728 distributions was assessed using the Shapiro-Wilks normality test before choosing parametric
729 (Student's *t* test) or a non-parametric (Mann-Whitney) tests, as indicated in relevant figure
730 legends. Graphs were plotted using the PlotsOfData service[46].
731

FIGURE LEGENDS

Figure 1. Ion channel localization reveals elaborate muscle membrane compartmentalization

(A) Schematic diagram of the organization of the *C. elegans* musculature in the head and midbody region. Dorso-ventral view of two out of four muscle quadrants. Successive muscle cells are labeled in green and grey. Anterior (*Ant*) to the left, posterior (*Pos*) to the right.
(B) Asymmetric localization of TWK-28, TWK-24 and SLO-1 channels. Muscle membrane labeled by TWK-12-wrmScarlet, magenta.
(C) Image segmentation reveals little to no co-localization of ion channels in triple-labeled muscle cell using TWK-28 (cyan), TWK-24 (magenta), and SLO-1(green) fluorescent knockin lines.
(D) SLO-1 and ISLO-1 distributions overlap exclusively in the posterior domain. ISLO-1 is also found in the anterior domain of the muscle cell.
(E) TWK-28 and ISLO-1 distributions overlap in the anterior domain of muscle cells. Rightmost column, magnified view of anterior region of individual muscle cells.
Regions of interest in (D) and (E): *Anterior domain*, comet-like domain at anterior tip of muscle cells; *Posterior domain,* punctate clustered pattern in posterior part of muscle cells.
Muscle cell outlines are indicated with yellow dashed lines. Scale bars, 20 µm.

Figure 2. TWK-28 surface expression is dependent on dystrophin and DAPC-associated proteins

(A) Confocal detection and quantification of mNeonGreen-TWK-28 in a *dys-1* molecular null allele *(syb2174)* and a long-isoform-specific *dys-1* mutant *(bln582)*.
(B) Confocal detection and quantification of mNeonGreen-TWK-28 in *dyb-1(cx36)* and *islo-1(bln549)* loss-of-function mutants.
(C) C-terminal sequence of the TWK-28ΔPDZ variant engineered by gene editing of mNeonGreen-TWK-28 to eliminate a putative PDZ-binding motif (orange residues).
(D) Confocal detection and quantification of mNeonGreen-TWK-28 in *stn-1(ok292)* and *stn-2(ok2417)* loss-of-function mutants, and of an mNeonGreen-TWK-28 knockin line lacking the final four C-terminal amino acids (*twk-28ΔPDZ*).
(E) Confocal detection and quantification of mNeonGreen-TWK-28 and mNeonGreen-*twk-28ΔPDZ* in a *dys-1(syb2174)* molecular null allele.
(F) TWK-8, TWK-18, TWK-24, and TWK-42 expression and subcellular distributions are unchanged in *dys-1(bln582)* loss-of-function mutant. Representative images of head musculature.
(G) DYS-1 degradation protocol. L4 (P0) worms are transferred to auxin-containing media at day 0 (D0). F1 progeny are exposed to auxin until the L4 stage (ON Auxin) and transferred to NGM plates (OFF Auxin) for 24h. Confocal detection and quantification of fluorescence at day 3 (D3) and 24 hours later (D3 + 24h).
(H) DYS-1-AID-mNeonGreen is strongly degraded after lifelong exposure to auxin (ON Auxin, D3). Partial recovery 24 h after removal from auxin (OFF Auxin, D3 + 24h).
(I), (J) Confocal detection of wrmScarlet-TWK-28 and DYS-1-AID-mNeonGreen at D3 and D3 + 24h, in the absence of auxin (NO Auxin, age-matched controls), after auxin exposure for three days (ON Auxin), and after removal from auxin for 24h (OFF Auxin).
(K) Quantification of wrmScarlet-TWK-28 fluorescence.
Mann-Whitney test, n > 30 in all samples; n.s., not significant, * $p < 0.05$
Scale bars, 20 µm

Figure 3. Dystrophin, dystroglycan and sarcoglycans define asymmetrical membrane compartments at the surface of *C. elegans* muscle cells

(A) DGN-1 and DYS-1 distributions overlap in body wall muscle cells.

(B) DGN-1 localizes to sarcolemmal domains devoid of α-integrins/PAT-2. Representative images of head muscle cells of DGN-1-wrmScarlet (in magenta) and PAT-2-mNeonGreen (in green) translational fusion knockin lines.

(C), (D) DGN-1 and PAT-2 occupy juxtaposed and optically-separable membrane domains. Enlargement of images shown in panel B.

(E) SGCB-1 and DYS-1 distributions overlap only partially in body wall muscle cells.

(F) SGCB-1 partitions into distinct membrane domains along the antero-posterior axis of individual muscle cells. *Anterior domain*, comet-like domain. *Gap domain,* sparse localization. *Posterior domain,* clustered pattern aligned with, but optically-separable from, PAT-2-labeled dense bodies.

(G) DGN-1 and SGCB-1 patterns only partially coincide in the anterior and posterior regions of muscle cells.

Muscle cell outlines are indicated with yellow dashed lines. Scale bars, 20 µm.

Figure 4. Loss of DSH-1/disheveled disrupts the planar-polarized organization of the muscle plasma membrane

(A), (B) Symmetrical distribution of TWK-28, SLO-1 and TWK-24 in *dsh-1(ok1445)* loss-of-function background. Muscle membrane labeled by TWK-12-wrmScarlet, magenta.

(B) Magnified view of single muscle cells in wild type and *dsh-1(ok1445)*.

(C) Quantification of TWK-28, SLO-1 and TWK-24 domain boundary positions in wild type and *dsh-1(ok1445)*. Average position of anterior (*Ant*) boundaries in wild type (black) and *dsh-1(ok1445)* (red), respectively, as percentages of muscle cell length: TWK-28, 31% and 30%; SLO-1, 24% and 23%; TWK-24, 23% and 21%. Average position of posterior (*Pos)* boundaries in wild type and *dsh-1(ok1445)*, respectively, as percentages of muscle cell length: TWK-28, 97% and 73%; SLO-1, 90% and 78%; TWK-24, 68% and 80%. Gray and red bars indicate the region containing each ion channel. Number of cells assayed in each condition: TWK-28 (WT, n=29; *dsh-1*, n=25); SLO-1 (WT, n=30; *dsh-1*, n=26); TWK-24 (WT, n=33; *dsh-1*, n=26).

(D) Image segmentation reveals little to no co-localisation of ion channels in *dsh-1*-mutant muscle cell using TWK-28 (cyan), TWK-24 (magenta), and SLO-1(green) fluorescent knockin lines.

(E) Total TWK-28 surface expression is unchanged in *dsh-1(ok1445)* as TWK-28 is redistributed between the anterior and posterior domains. Mann-Whitney test, n.s. non-significant, * $p < 0.05$.

(F) Symmetrical distribution of DYS-1 and TWK-28 at extremities of muscle cells in *dsh-1(ok1445)*.

(G) Symmetrical distribution of SGCB-1 in *dsh-1(ok1445)*.

(H) Symmetrical distribution TWK-28 lacking the PDZ binding-motif in *dsh-1(ok1445)*. White arrowhead indicate remaining fluorescent signal.

Muscle cell outlines are indicated with yellow dashed lines. Scale bars, 20 µm.

Figure 5. Loss of MIG-14/Wntless, EGL-20/Wnt and CAM-1/Ror disrupts asymmetric localization of TWK-28

(A) Schematic protein structure of DSH-1a including DIX, PDZ, DEP domains.

(B) Muscle-specific expression of full-length or DIX domain-truncated DSH-1a proteins rescues TWK-28 localization in *dsh-1(ok1445)*. PDZ and DEP domains are necessary for DSH-1 function.
(C) Planar-polarized distribution of TWK-28 is maintained in the absence of core planar cell polarity components (*vang-1, fmi-1, prkl-1*), Cadherin/Fat/Dachsous pathway components (*cdh-1, cdh-3, cdh-4*), or β-catenin (*bar-1*).
(D) Loss of MIG-14/Wntless, EGL-20/Wnt, and CAM-1/Ror disrupts polarized localization of TWK-28. Anterior mid-body muscle cells in *mig-14*, *cam-1* and *egl-20* mutants are wild type. Posterior mid-body muscle cells are affected in all mutant genotypes.
(E) Schematic protein structure of CAM-1/Ror receptor, with corresponding molecular lesions in point mutants (*gm122* and *cw82)*, and deletion alleles (*ak37* and *ks52*).
(F) *cam-1(ak37), cam-1(ks52)* and *cam-1(cw82)* disrupt TWK-28 localization in posterior mid-body muscles.
Left- or right-pointing yellow arrowheads indicate anterior or posterior extremity of muscle cells, respectively. Scale bars, 20 μm.

Figure 6. DSH-1/disheveled is required to establish and maintain muscle membrane polarity

(A) Representative micrograph of a DSH-1 mNeonGreen translational knockin line. DSH-1 is enriched in the posterior portion of body wall muscle cells. DSH-1::mNeonGreen is visible in ventral nerve cord motoneuron cell bodies and neurites. Ventral view.
(B) DSH-1::mNeonGreen distribution in a single muscle cells. Muscle membrane labeled by TWK-12-wrmScarlet, magenta. Average position of DSH-1 domain boundary, 72 % of muscle cell length, n=29. *Ant*, anterior. *Pos*, posterior. Gray bar indicates the region containing DSH-1.
(C) DSH-1 and TWK-28 are found at opposite ends of muscle cells. Yellow or white arrowheads and dashed lines indicate the anterior or posterior end of muscle cells, respectively.
(D) Asymmetric localization of TWK-28 in L1, L2, and L3 larval stages. Non-polarized muscle cells are found in wild-type at the L1 stage. Loss of *dsh-1* disrupts muscle cell polarity at all stages. Muscle cells are labeled with cytoplasmic mCherry in the L1 stage and outlined with white dotted lines.
(E) DSH-1 is required to maintain muscle polarity during post-embryonic development.
(F) Defective muscle polarity is restored by re-expression of DSH-1 during post-embryonic development.
White arrow heads indicate the posterior end of muscle cells in (A), (B), and (C).
Left- or right-pointing yellow arrowheads indicate anterior or posterior extremity of muscle cells, respectively. Scale bars, 20 μm.

SUPPLEMENTARY FIGURE LEGENDS

Figure S1. Genetic suppression of a TWK-28 L210T gain-of-function mutant by mutations in *dys-1* and *islo-1*

(A) Two-pore domain potassium channels TWK-12 and TWK-43 are enriched in muscle arms and on the lateral membrane of muscle cells.
(B) Current–voltage relationships obtained at pH 7.4 in *X. laevis* oocytes after injection of cRNA encoding TWK-28 wild-type (black squares) and TWK-28 L210T TM2.6 mutant channels (red squares). Inset shows leftward shift of reversal potential in TWK-28 L210T. n=8 and n=7 for wild-type and TWK-28 L210T, respectively.
(C) Low and high magnification micrographs illustrating reduced locomotion and relaxed body posture of *twk-28(L210T)* gain-of-function mutants on NGM plates.
(D) Loss-of-function mutations in *dys-1* and a missense mutation in *islo-1* suppress paralysis of the TWK-28 L210T gain-of-function mutation.
(E) TWK-28 surface expression is unchanged in sarcoglycan single or triple null mutants.
(F) Quantification of TWK-28-associated fluorescence. Mann-Whitney test; n.s., not significant.
Scale bar, 20 µm

Figure S2. Dystrophin is required for sarcolemmal localization of dystroglycan and sarcoglycans.

(A), (B) Sarcoglycans SGCA-1 and SGN-1 are colocalized with SGCB-1.
(C) Subunit interdependence for surface expression of SGCA-1, SGCB-1 and SGN-1.
(D) SGBC-1 localization is disrupted differently in *dys-1* and *dyb-1* mutants.
(E) Reduction in surface expression and mislocalization of DGN-1 in perlecan/*unc-52* loss of function mutants.
(F) DGN-1 localization is dependent on DYS-1, but not DYB-1.
Scale bars, 20 µm.

Figure S3. Relative localization of DAPC component in *C. elegans* head muscles

(A) Colocalization of DGN-1 and STN-2.
(B) Colocalization of SGCB-1 and DYB-1.
(C) Colocalization of SGCB-1 and STN-1.
(D) Colocalization of DGN-1 and DYB-1.
(E) Colocalization of STN-1 and STN-2.
Muscle cell outlines are indicated with yellow dashed lines. Scale bars, 20 µm.

Figure S4. DAPC components partition to dystroglycan- or sarcoglycan-containing membrane compartments

(A) Colocalization of DGN-1 and DYS-1.
(B) Colocalization of DGN-1 and STN-2.
(C) Colocalization of SGCB-1 and DYB-1.
(D) Colocalization of SGCB-1 and STN-1.
(E) Colocalization of DGN-1 and DYB-1.
(F) Colocalization of SGCB-1 and DYS-1.
(G) Colocalization of STN-1 and STN-2.
Anterior domain, comet-like domain at anterior tip of muscle cells; *Posterior domain,* punctate clustered pattern in posterior part of muscle cells.

Figure S5. TWK-28 colocalizes with all DAPC components

Colocalization of TWK-28 with SGCB-1, STN-1, DYB-1, DGN-1, DYS-1 and STN-2. Rightmost column, magnified view of anterior region of individual muscle cells.
Scale bars, 20 µm.

Figure S6. EGL-20/Wnt is required for muscle cell polarity while several Wnt ligands and receptors are not

(A), (B) Wnt ligands (*cwn-1, cwn-2, lin-44*), frizzled receptors (*lin-17, mig-1, cfz-2*) and the tyrosine kinase-related receptors LIN-18/Ryk are not required for TWK-28 planar polarization. (C) *egl-20(bln916)* –an early nonsense mutation at position Pro21– disrupts TWK-28 localization in posterior midbody muscles.
Scale bars, 20 µm.

Figure S7. The localization of DSH-1 is dependent on CAM-1 and EGL-20

(A) Enrichment of DSH-1 at the posterior end of muscle cells is lost in *cam-1* and *egl-20* mutants. DSH-1 localization is however conserved in the anterior midbody of *egl-20* mutants, consistent with the posteriorly-restricted distribution of EGL-20. White arrow heads indicate DSH-1 enrichment at the posterior end of muscle cells. Ventral view.
(B) Life-long degradation of DSH-1-AID-mNeonGreen using an ubiquitous TIR1-expressing transgene disrupts asymmetric localization of TWK-28 in muscle cells.
Scale bars, 20 µm.

REFERENCES

1. Bennett, V., and Lorenzo, D.N. (2016). An Adaptable Spectrin/Ankyrin-Based Mechanism for Long-Range Organization of Plasma Membranes in Vertebrate Tissues. Current topics in membranes *77*, 143–184. 10.1016/bs.ctm.2015.10.001.

2. Bennett, V., and Lorenzo, D.N. (2013). Spectrin- and ankyrin-based membrane domains and the evolution of vertebrates. Current topics in membranes *72*, 1–37. 10.1016/b978-0-12-417027-8.00001-5.

3. Connors, N.C., Adams, M.E., Froehner, S.C., and Kofuji, P. (2004). The Potassium Channel Kir4.1 Associates with the Dystrophin-Glycoprotein Complex via α-Syntrophin in Glia*. J Biol Chem *279*, 28387–28392. 10.1074/jbc.m402604200.

4. Gavillet, B., Rougier, J.-S., Domenighetti, A.A., Behar, R., Boixel, C., Ruchat, P., Lehr, H.-A., Pedrazzini, T., and Abriel, H. (2006). Cardiac Sodium Channel Nav1.5 Is Regulated by a Multiprotein Complex Composed of Syntrophins and Dystrophin. Circ Res *99*, 407–414. 10.1161/01.res.0000237466.13252.5e.

5. Lai, H.C., and Jan, L.Y. (2006). The distribution and targeting of neuronal voltage-gated ion channels. Nat Rev Neurosci *7*, 548–562. 10.1038/nrn1938.

6. Yang, Y., and Mlodzik, M. (2015). Wnt-Frizzled/Planar Cell Polarity Signaling: Cellular Orientation by Facing the Wind (Wnt). Annu Rev Cell Dev Bi *31*, 623–646. 10.1146/annurev-cellbio-100814-125315.

7. Gieseler, K., Qadota, H., and Benian, G.M. (2017). Development, structure, and maintenance of C. elegans body wall muscle.

8. Mizumoto, K., Jin, Y., and Bessereau, J.-L. (2023). Synaptogenesis: unmasking molecular mechanisms using Caenorhabditis elegans. Genetics *223*. 10.1093/genetics/iyac176.

9. Kim, H., Pierce-Shimomura, J.T., Oh, H.J., Johnson, B.E., Goodman, M.B., and McIntire, S.L. (2009). The Dystrophin Complex Controls BK Channel Localization and Muscle Activity in Caenorhabditis elegans. Plos Genet *5*, e1000780. 10.1371/journal.pgen.1000780.

10. Sancar, F., Touroutine, D., Gao, S., Oh, H.J., Gendrel, M., Bessereau, J.-L., Kim, H., Zhen, M., and Richmond, J.E. (2011). The dystrophin-associated protein complex maintains muscle excitability by regulating Ca(2+)-dependent K(+) (BK) channel localization. Journal of Biological Chemistry *286*, 33501–33510. 10.1074/jbc.m111.227678.

11. Cao, J., Packer, J.S., Ramani, V., Cusanovich, D.A., Huynh, C., Daza, R., Qiu, X., Lee, C., Furlan, S.N., Steemers, F.J., et al. (2017). Comprehensive single-cell transcriptional profiling of a multicellular organism. Science *357*, 661–667. 10.1126/science.aam8940.

12. Vigne, P., Gimond, C., Ferrari, C., Vielle, A., Hallin, J., Pino-Querido, A., El Mouridi, S, Frøkjær-Jensen, C., Boulin, T., Teotónio, H., et al. (2020). A single nucleotide change underlies the genetic assimilation of a plastic trait. bioRxiv, 2020.06.29.176990.

13. Kunkel, M.T., Johnstone, D.B., Thomas, J.H., and Salkoff, L. (2000). Mutants of a temperature-sensitive two-P domain potassium channel. The Journal of neuroscience : the official journal of the Society for Neuroscience *20*, 7517–7524.

14. Cruz, I.P. de la, Levin, J.Z., Cummins, C., Anderson, P., and Horvitz, H.R. (2003). sup-9, sup-10, and unc-93 may encode components of a two-pore K+ channel that coordinates muscle contraction in Caenorhabditis elegans. Journal of Neuroscience *23*, 9133–9145.

15. El Mouridi, S., Lecroisey, C., Tardy, P., Mercier, M., Leclercq-Blondel, A., Zariohi, N., and Boulin, T. (2017). Reliable CRISPR/Cas9 Genome Engineering in Caenorhabditis elegans Using a Single Efficient sgRNA and an Easily Recognizable Phenotype. G3 Genes Genomes Genetics *7*, 1429–1437. 10.1534/g3.117.040824.

16. Oh, K.H., Haney, J.J., Wang, X., Chuang, C.-F., Richmond, J.E., and Kim, H. (2017). ERG-28 controls BK channel trafficking in the ER to regulate synaptic function and alcohol response in C. elegans. eLife *6*, e1001077. 10.7554/elife.24733.

17. Taylor, S.R., Santpere, G., Weinreb, A., Barrett, A., Reilly, M.B., Xu, C., Varol, E., Oikonomou, P., Glenwinkel, L., McWhirter, R., et al. (2021). Molecular topography of an entire nervous system. Cell *184*, 4329-4347.e23. 10.1016/j.cell.2021.06.023.

18. Carre-Pierrat, M., Grisoni, K., Gieseler, K., Mariol, M.-C., Martin, E., Jospin, M., Allard, B., and Ségalat, L. (2006). The SLO-1 BK channel of Caenorhabditis elegans is critical for muscle function

994 and is involved in dystrophin-dependent muscle dystrophy. J Mol Biol *358*, 387–395.
995 10.1016/j.jmb.2006.02.037.

996 19. Kim, H., Pierce-Shimomura, J.T., Oh, H.J., Johnson, B.E., Goodman, M.B., and McIntire, S.L.
997 (2009). The dystrophin complex controls bk channel localization and muscle activity in Caenorhabditis
998 elegans. PLoS Genetics *5*, e1000780. 10.1371/journal.pgen.1000780.

999 20. Ben Soussia, I., El Mouridi, S., Kang, D., Leclercq-Blondel, A., Khoubza, L., Tardy, P., Zariohi, N.,
1000 Gendrel, M., Lesage, F., Kim, E.-J., et al. (2019). Mutation of a single residue promotes gating of
1001 vertebrate and invertebrate two-pore domain potassium channels. Nature communications *10*, 787.
1002 10.1038/s41467-019-08710-3.

1003 21. Hui, S., Xing, X., and Bader, G.D. (2013). Predicting PDZ domain mediated protein interactions
1004 from structure. Bmc Bioinformatics *14*, 27. 10.1186/1471-2105-14-27.

1005 22. Zhang, L., Ward, J.D., Cheng, Z., and Dernburg, A.F. (2015). The auxin-inducible degradation
1006 (AID) system enables versatile conditional protein depletion in C. elegans. Development *142*, 4374–
1007 4384. 10.1242/dev.129635.

1008 23. Grisoni, K., Martin, E., Gieseler, K., Mariol, M.-C., and Ségalat, L. (2002). Genetic evidence for a
1009 dystrophin-glycoprotein complex (DGC) in Caenorhabditis elegans. Gene *294*, 77–86. 10.1016/s0378-
1010 1119(02)00762-x.

1011 24. Johnson, R.P., Kang, S.H., and Kramer, J.M. (2006). C. elegans dystroglycan DGN-1 functions in
1012 epithelia and neurons, but not muscle, and independently of dystrophin. Development *133*, 1911–
1013 1921. 10.1242/dev.02363.

1014 25. Keeley, D.P., Hastie, E., Jayadev, R., Kelley, L.C., Chi, Q., Payne, S.G., Jeger, J.L., Hoffman,
1015 B.D., and Sherwood, D.R. (2020). Comprehensive Endogenous Tagging of Basement Membrane
1016 Components Reveals Dynamic Movement within the Matrix Scaffolding. Dev Cell *54*, 60-74.e7.
1017 10.1016/j.devcel.2020.05.022.

1018 26. Holt, K.H., and Campbell, K.P. (1998). Assembly of the Sarcoglycan Complex INSIGHTS FOR
1019 MUSCULAR DYSTROPHY*. J Biol Chem *273*, 34667–34670. 10.1074/jbc.273.52.34667.

1020 27. Talts, J.F., Andac, Z., Göhring, W., Brancaccio, A., and Timpl, R. (1999). Binding of the G domains
1021 of laminin α1 and α2 chains and perlecan to heparin, sulfatides, α-dystroglycan and several
1022 extracellular matrix proteins. Embo J *18*, 863–870. 10.1093/emboj/18.4.863.

1023 28. Ishikawa-Sakurai, M., Yoshida, M., Imamura, M., Davies, K.E., and Ozawa, E. (2004). ZZ domain
1024 is essentially required for the physiological binding of dystrophin and utrophin to β-dystroglycan. Hum
1025 Mol Genet *13*, 693–702. 10.1093/hmg/ddh087.

1026 29. Chung, W., and Campanelli, J.T. (1999). WW and EF Hand Domains of Dystrophin-Family
1027 Proteins Mediate Dystroglycan Binding. Mol Cell Biology Res Commun *2*, 162–171.
1028 10.1006/mcbr.1999.0168.

1029 30. Mullen, G.P., Rogalski, T.M., Bush, J.A., Gorji, P.R., and Moerman, D.G. (1999). Complex
1030 Patterns of Alternative Splicing Mediate the Spatial and Temporal Distribution of Perlecan/UNC-52 in
1031 Caenorhabditis elegans. Mol Biol Cell *10*, 3205–3221. 10.1091/mbc.10.10.3205.

1032 31. Cravo, J., and Heuvel, S. van den (2020). Tissue polarity and PCP protein function: C. elegans as
1033 an emerging model. Curr Opin Cell Biol *62*, 159–167. 10.1016/j.ceb.2019.11.004.

1034 32. Mlodzik, M. (2016). Chapter Five The Dishevelled Protein Family Still Rather a Mystery After Over
1035 20 Years of Molecular Studies. Curr Top Dev Biol *117*, 75–91. 10.1016/bs.ctdb.2015.11.027.

1036 33. Pani, A.M., and Goldstein, B. (2018). Direct visualization of a native Wnt in vivo reveals that a
1037 long-range Wnt gradient forms by extracellular dispersal. Elife *7*, e38325. 10.7554/elife.38325.

1038 34. Coudreuse, D.Y.M., Roël, G., Betist, M.C., Destrée, O., and Korswagen, H.C. (2006). Wnt
1039 Gradient Formation Requires Retromer Function in Wnt-Producing Cells. Science *312*, 921–924.
1040 10.1126/science.1124856.

1041 35. Belhasan, D.C., and Akaaboune, M. (2020). The role of the Dystrophin Glycoprotein Complex on
1042 the Neuromuscular System. Neurosci Lett *722*, 134833. 10.1016/j.neulet.2020.134833.

1043 36. Brouilly, N., Lecroisey, C., Martin, E., Pierson, L., Mariol, M.-C., Qadota, H., Labouesse, M.,
1044 Streichenberger, N., Mounier, N., and Gieseler, K. (2015). Ultra-structural time-course study in the C.
1045 elegans model for Duchenne muscular dystrophy highlights a crucial role for sarcomere-anchoring
1046 structures and sarcolemma integrity in the earliest steps of the muscle degeneration process. Hum
1047 Mol Genet *24*, 6428–6445. 10.1093/hmg/ddv353.

Figure 1

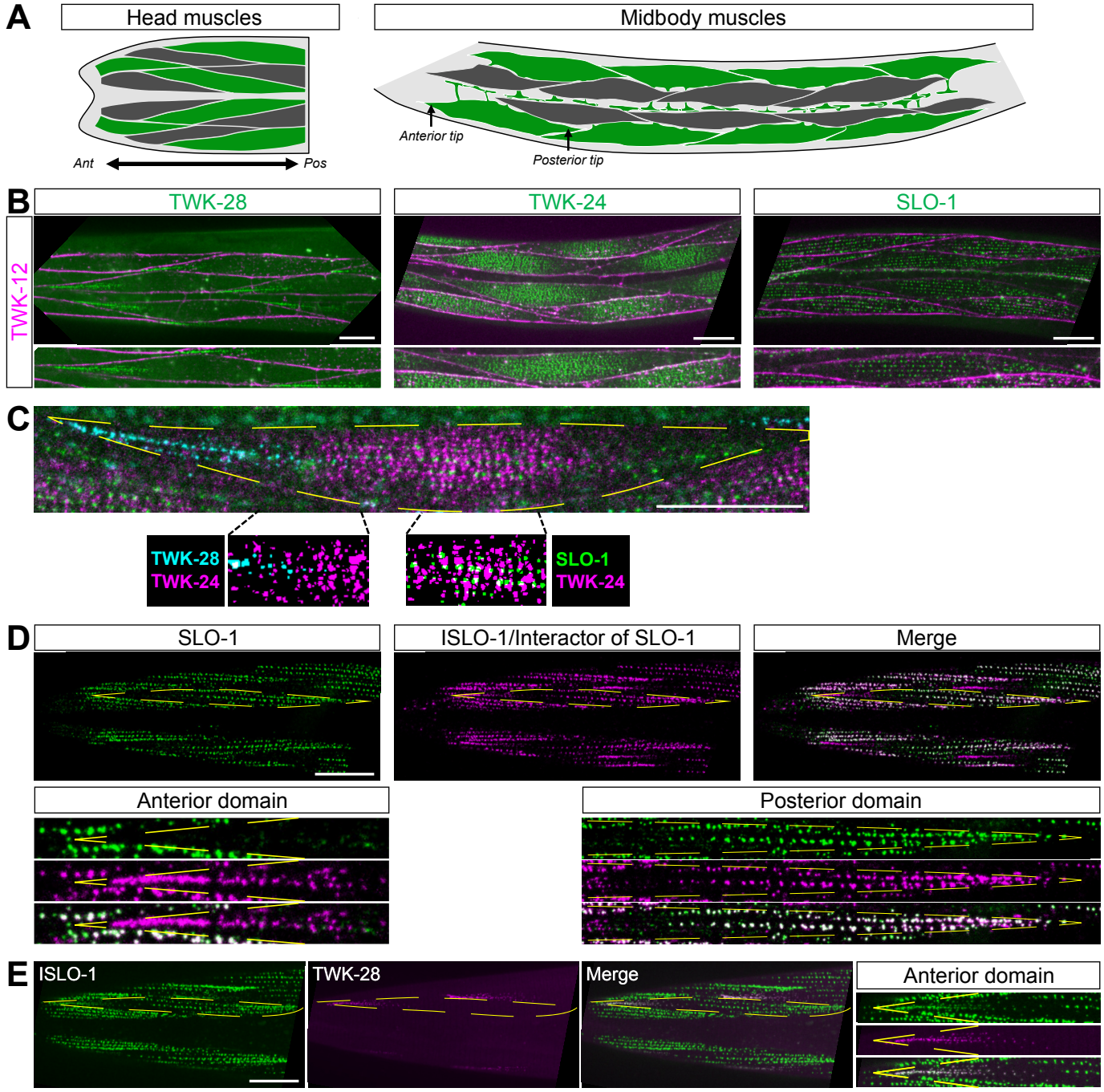

Figure 2

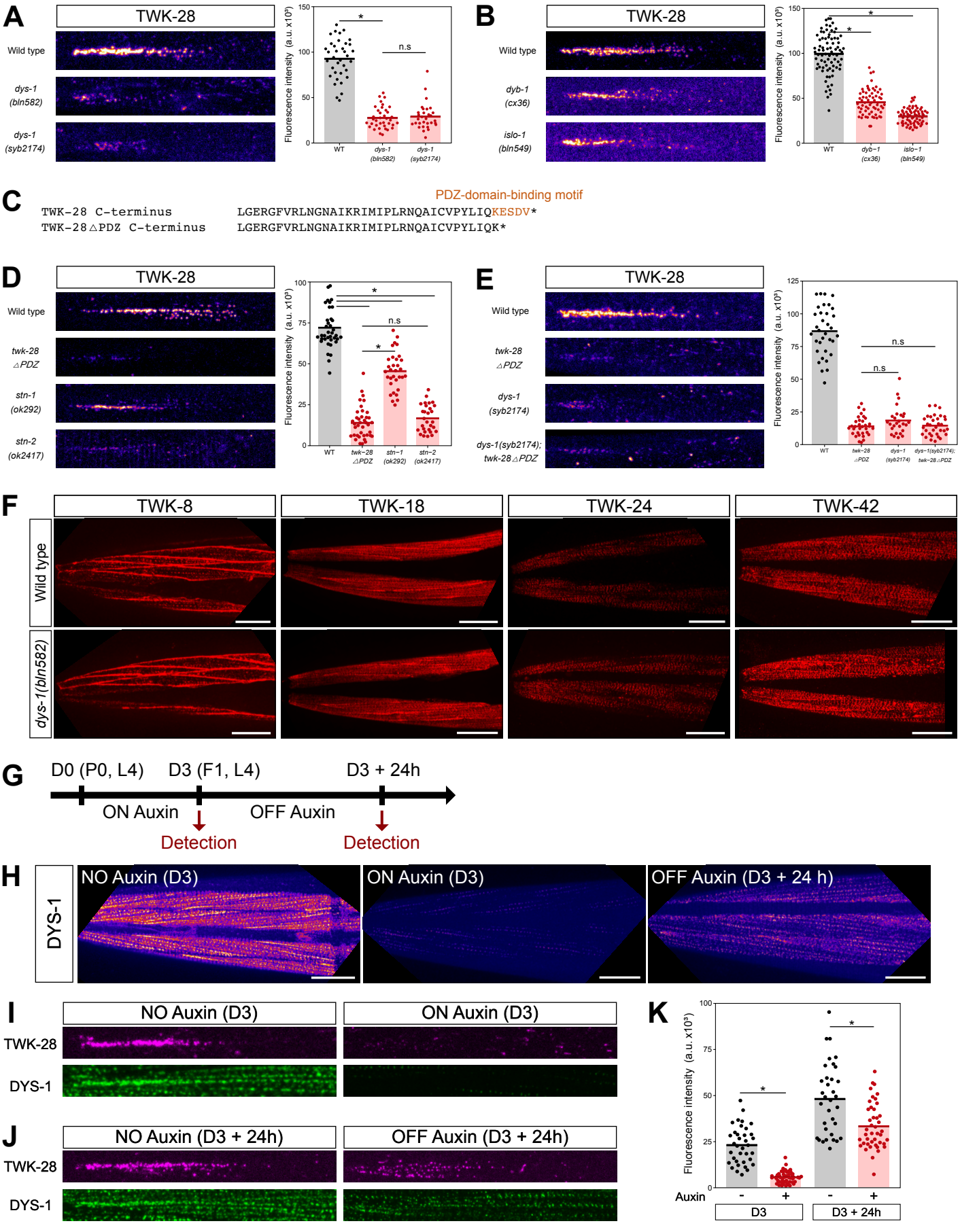

Figure 3

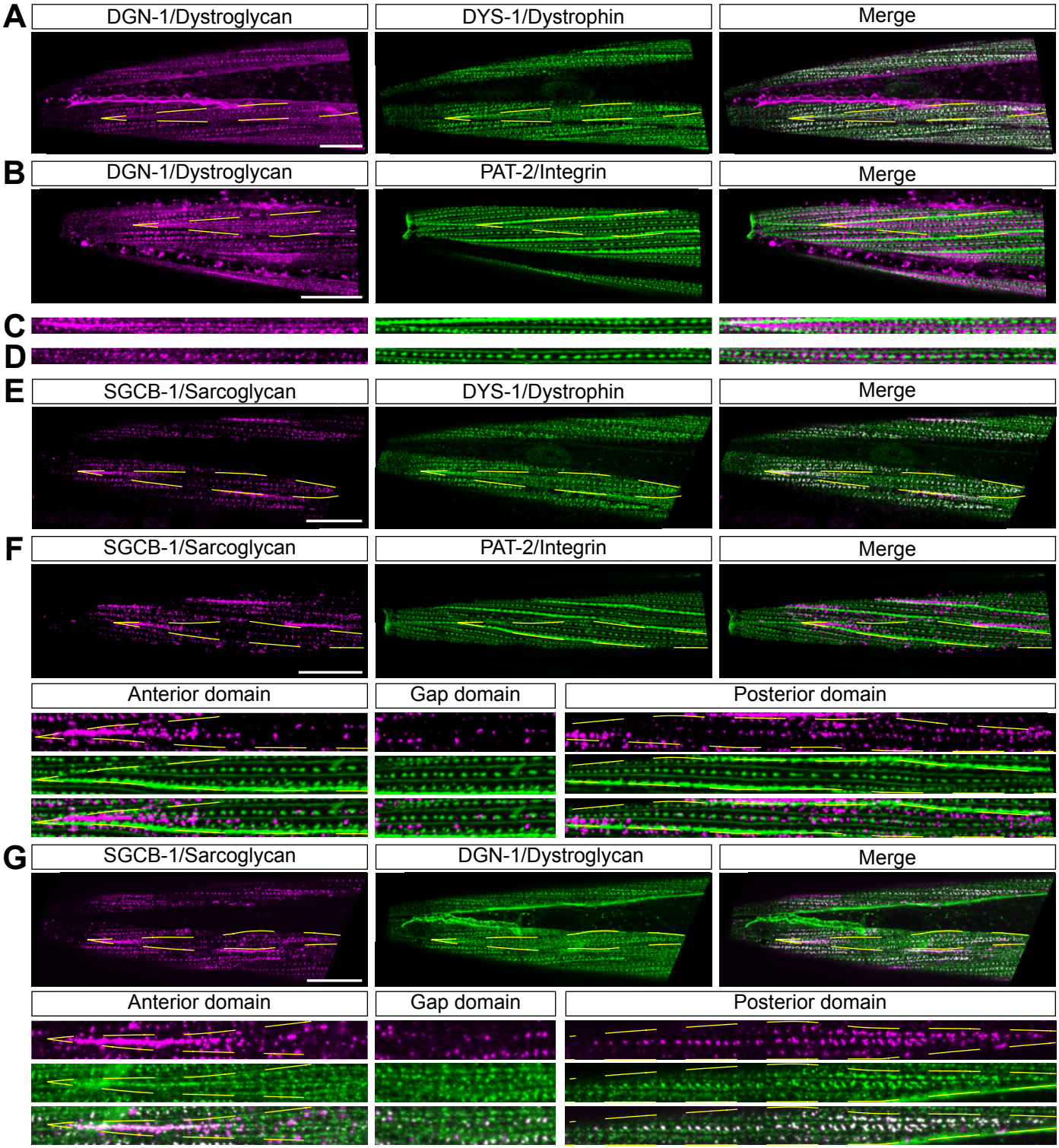

Figure 4

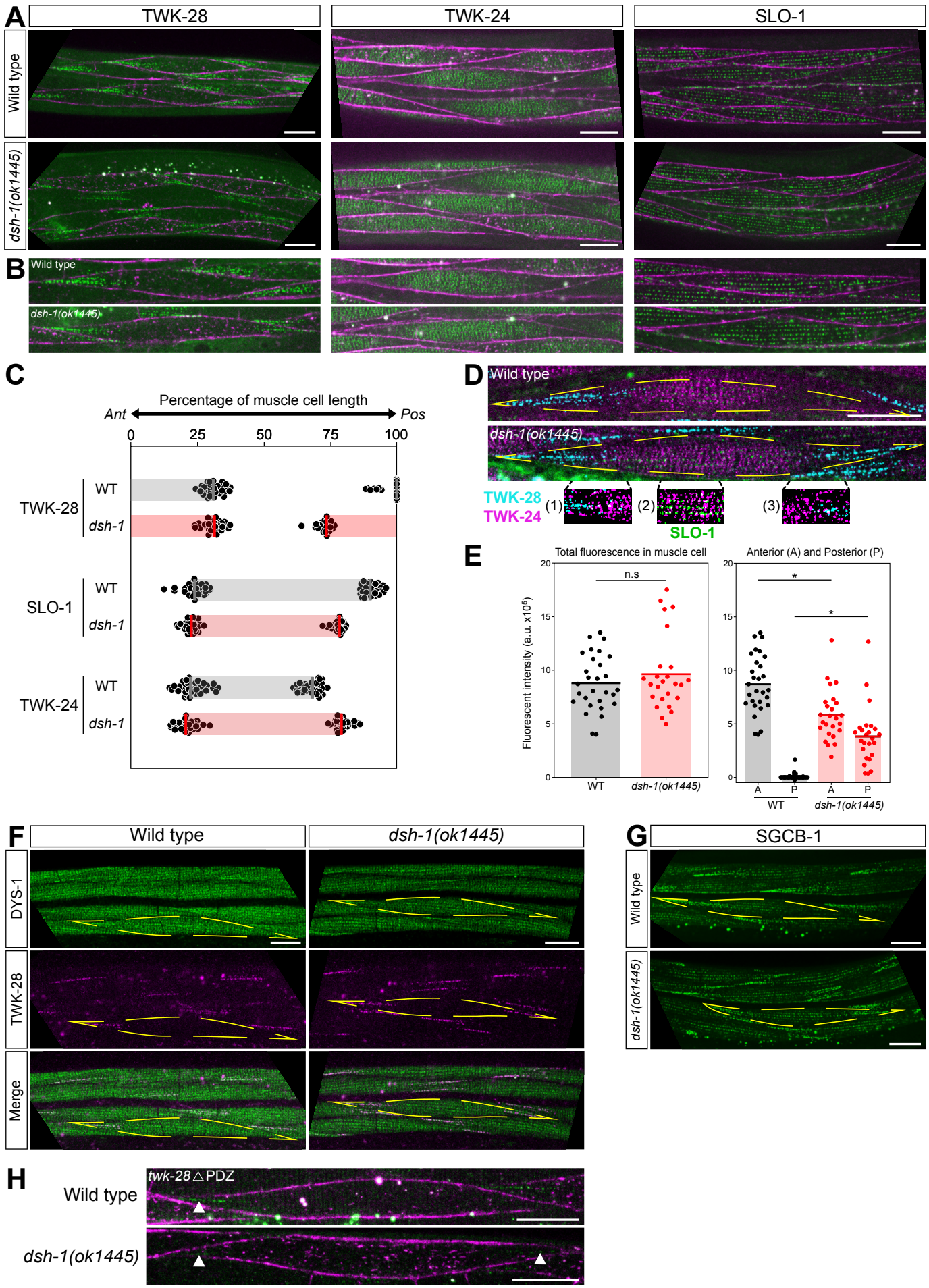

Figure 5

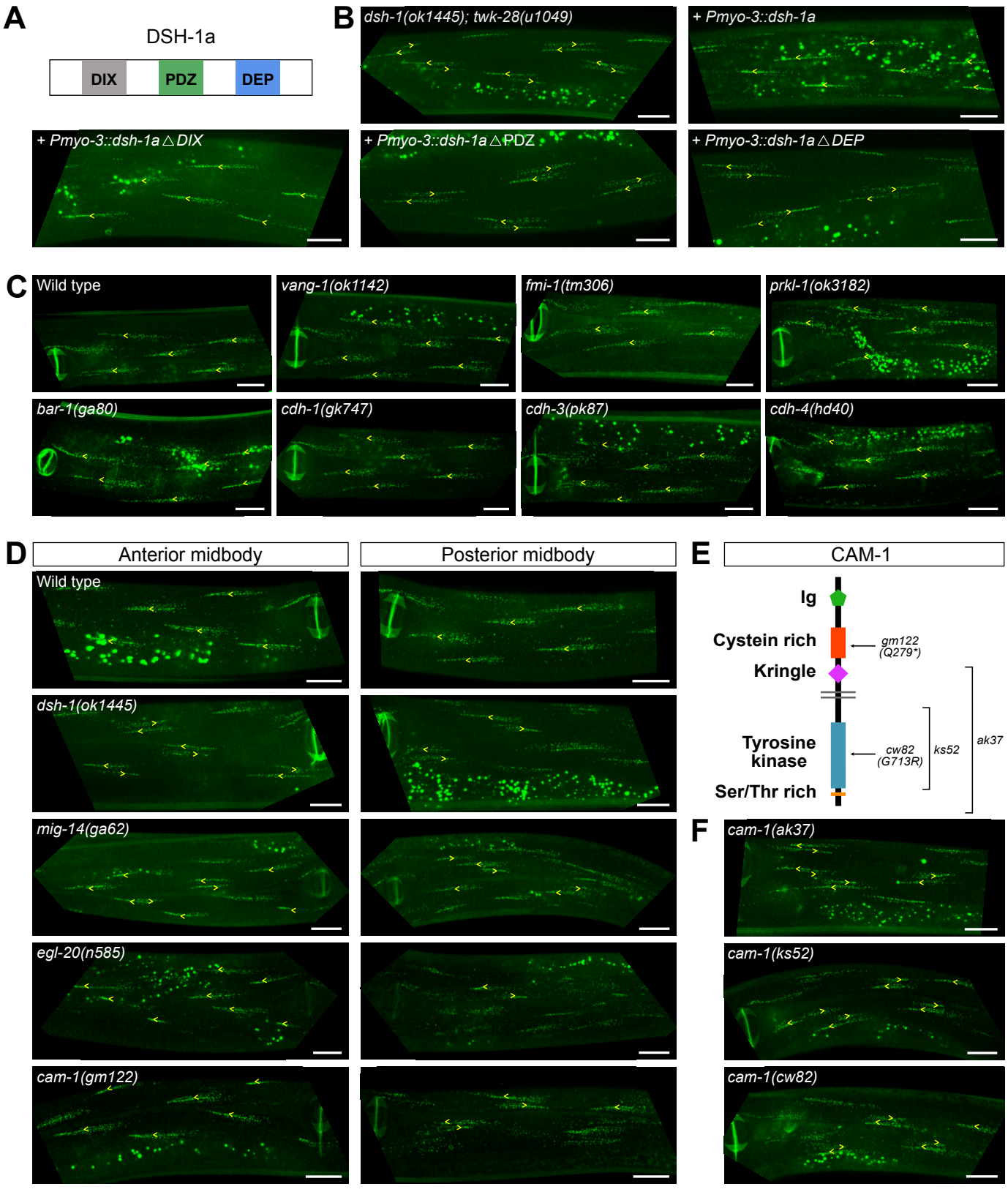
A
DSH-1a
DIX
PDZ
DEP
B
dsh-1(ok1445); twk-28(u1049)
+ Pmyo-3::dsh-1a
+ Pmyo-3::dsh-1a△DIX
+ Pmyo-3::dsh-1a△PDZ
+ Pmyo-3::dsh-1a△DEP
C
Wild type
vang-1(ok1142)
fmi-1(tm306)
prkl-1(ok3182)
bar-1(ga80)
cdh-1(gk747)
cdh-3(pk87)
cdh-4(hd40)
D
Anterior midbody
Posterior midbody
Wild type
dsh-1(ok1445)
mig-14(ga62)
egl-20(n585)
cam-1(gm122)
E
CAM-1
Ig
Cystein rich
Kringle
Tyrosine kinase
Ser/Thr rich
gm122 (Q279*)
cw82 (G713R)
ks52
ak37
F
cam-1(ak37)
cam-1(ks52)
cam-1(cw82)

Figure 6

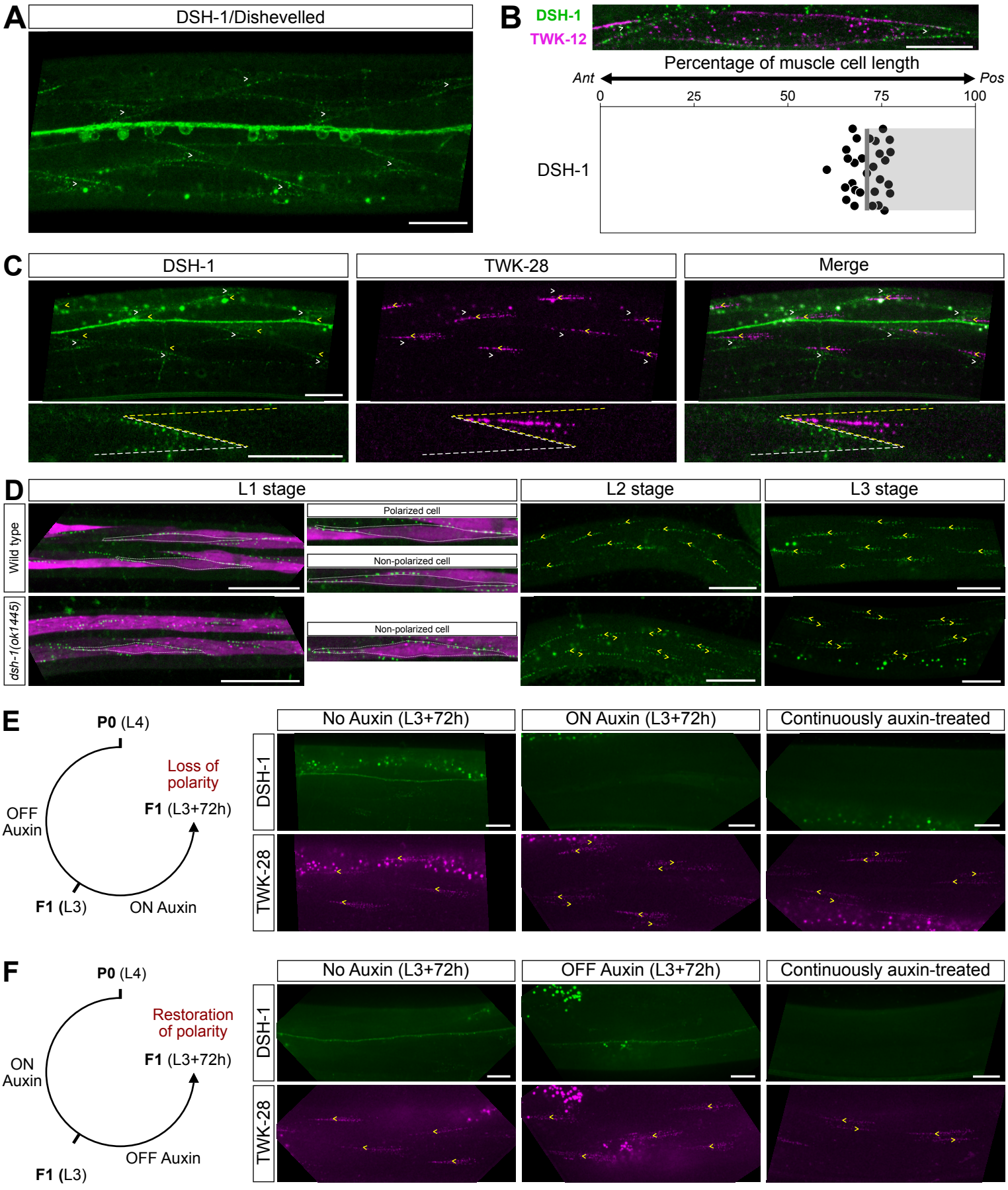

Figure S1

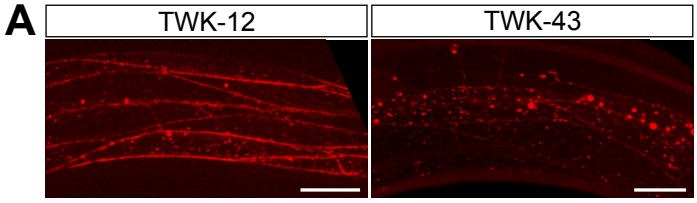

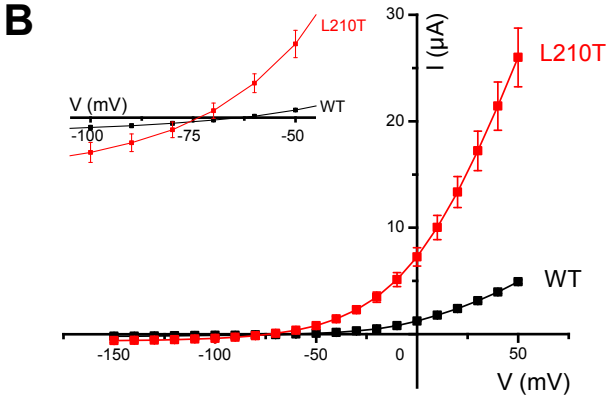

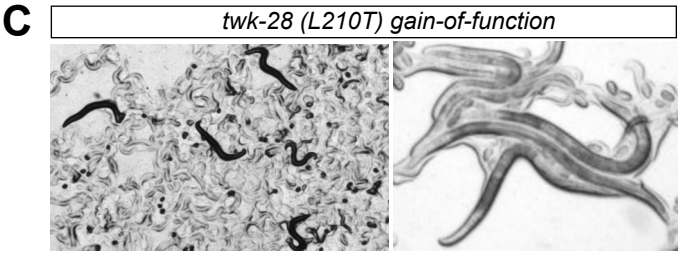

D

Allele	Locus	Mutation	Effect
bln557	*dys-1*	G to A ; ChrI:11556770	Q30Ochre
bln545	*dys-1*	C to T ; ChrI:11556616	W81Amber
bln582	*dys-1*	C to T ; ChrI:11556528	W110Opal
bln554	*dys-1*	C to T ; ChrI:11556280	W138Amber
bln583	*dys-1*	T to A ; ChrI:11544157	K1527Amber
bln568	*dys-1*	G to A ; ChrI:11543893	Q1615Ochre
bln552	*dys-1*	C to T ; ChrI:11540064	W2277Opal
bln571	*dys-1*	C to A ; ChrI:11538895	E2442Ochre
bln565	*dys-1*	C to T ; ChrI:11538087	W2582Opal
bln573	*dys-1*	G to A ; ChrI:11537052	Q2695Ochre
bln566	*dys-1*	C to T ; ChrI:11536816	W2773Opal
bln564	*dys-1*	C to T ; ChrI:11536387	W2807Amber
bln562	*dys-1*	G to A ; ChrI:11534654	Q2992Ochre
bln556	*dys-1*	G to A ; ChrI:11532291	loss of splice-donor
bln549	*islo-1*	G to A ; ChrIV:8137939	G165D

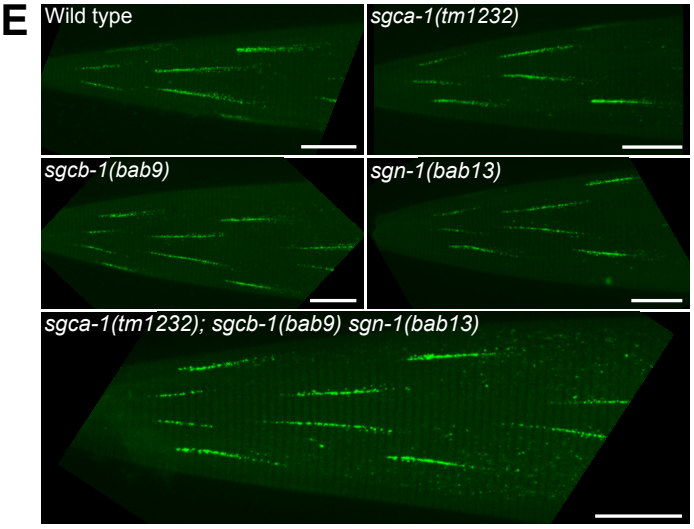

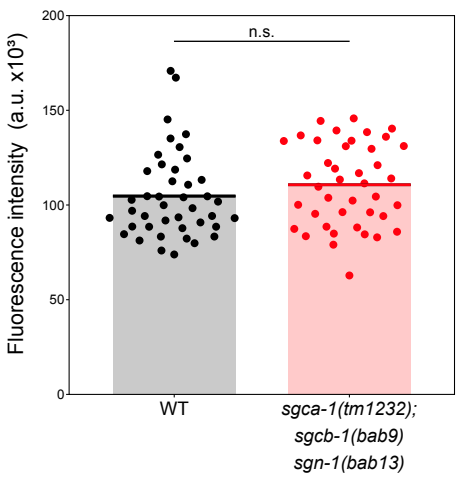

Figure S2

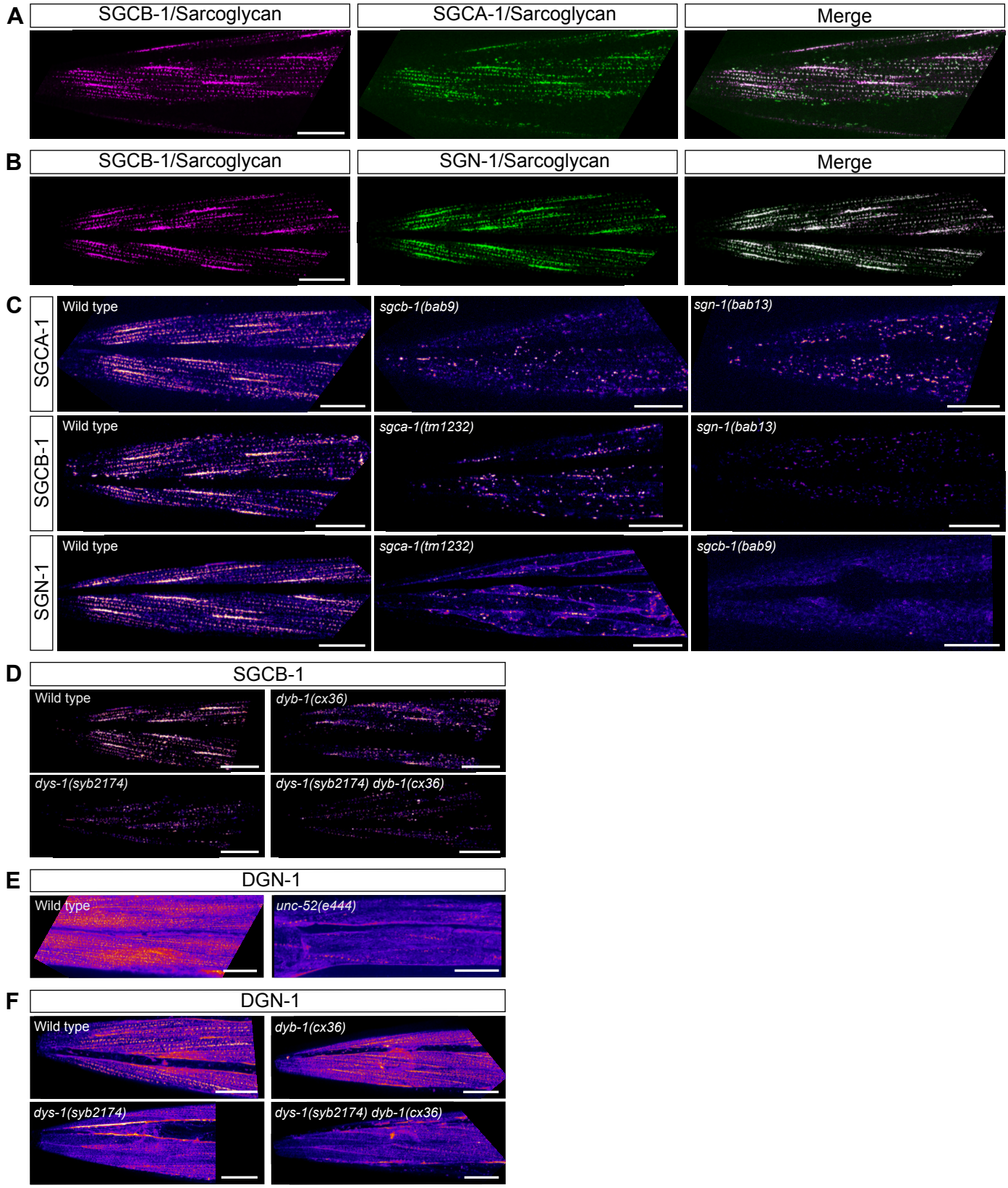

Figure S3

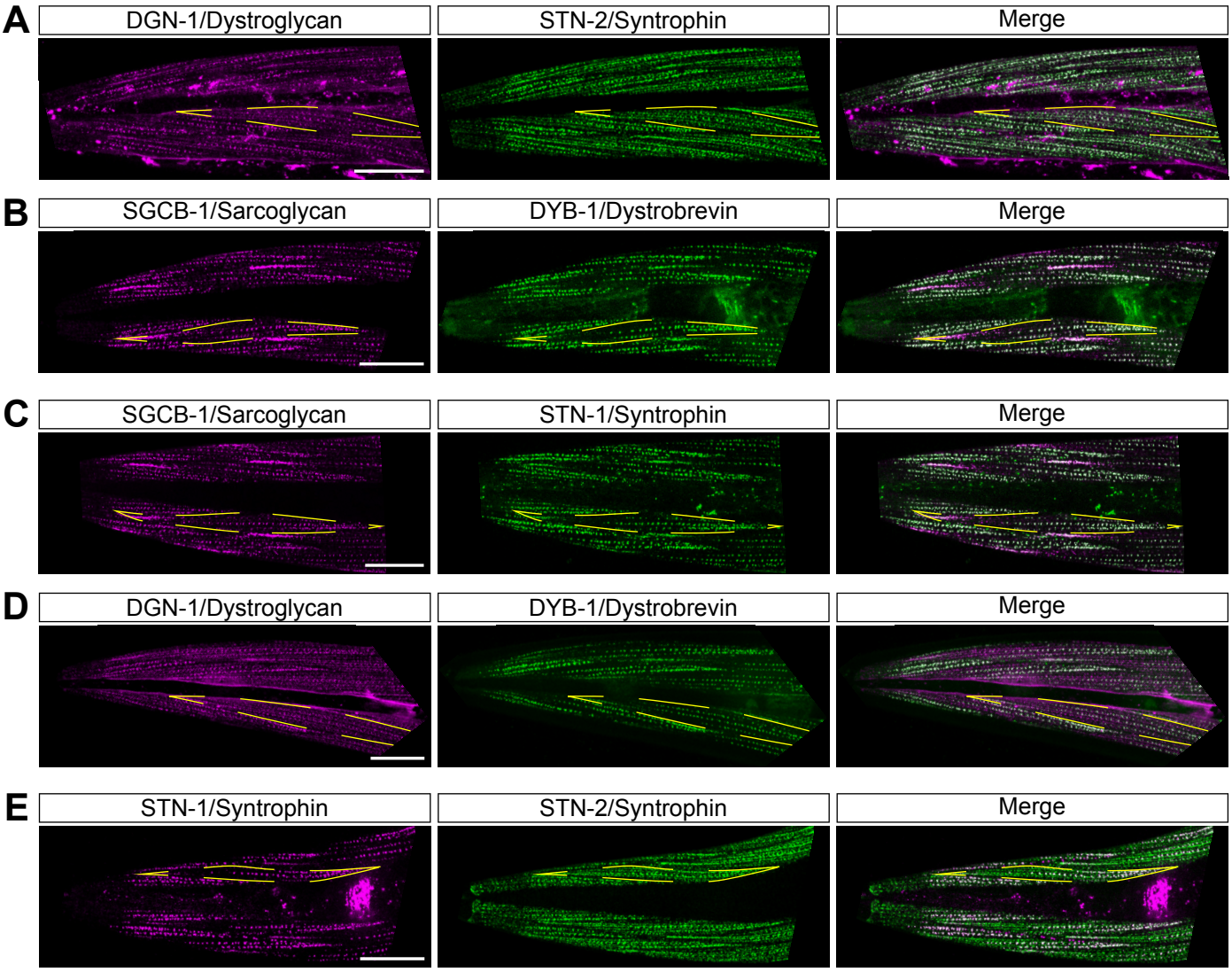
A
DGN-1/Dystroglycan
STN-2/Syntrophin
Merge
B
SGCB-1/Sarcoglycan
DYB-1/Dystrobrevin
Merge
C
SGCB-1/Sarcoglycan
STN-1/Syntrophin
Merge
D
DGN-1/Dystroglycan
DYB-1/Dystrobrevin
Merge
E
STN-1/Syntrophin
STN-2/Syntrophin
Merge

Figure S4

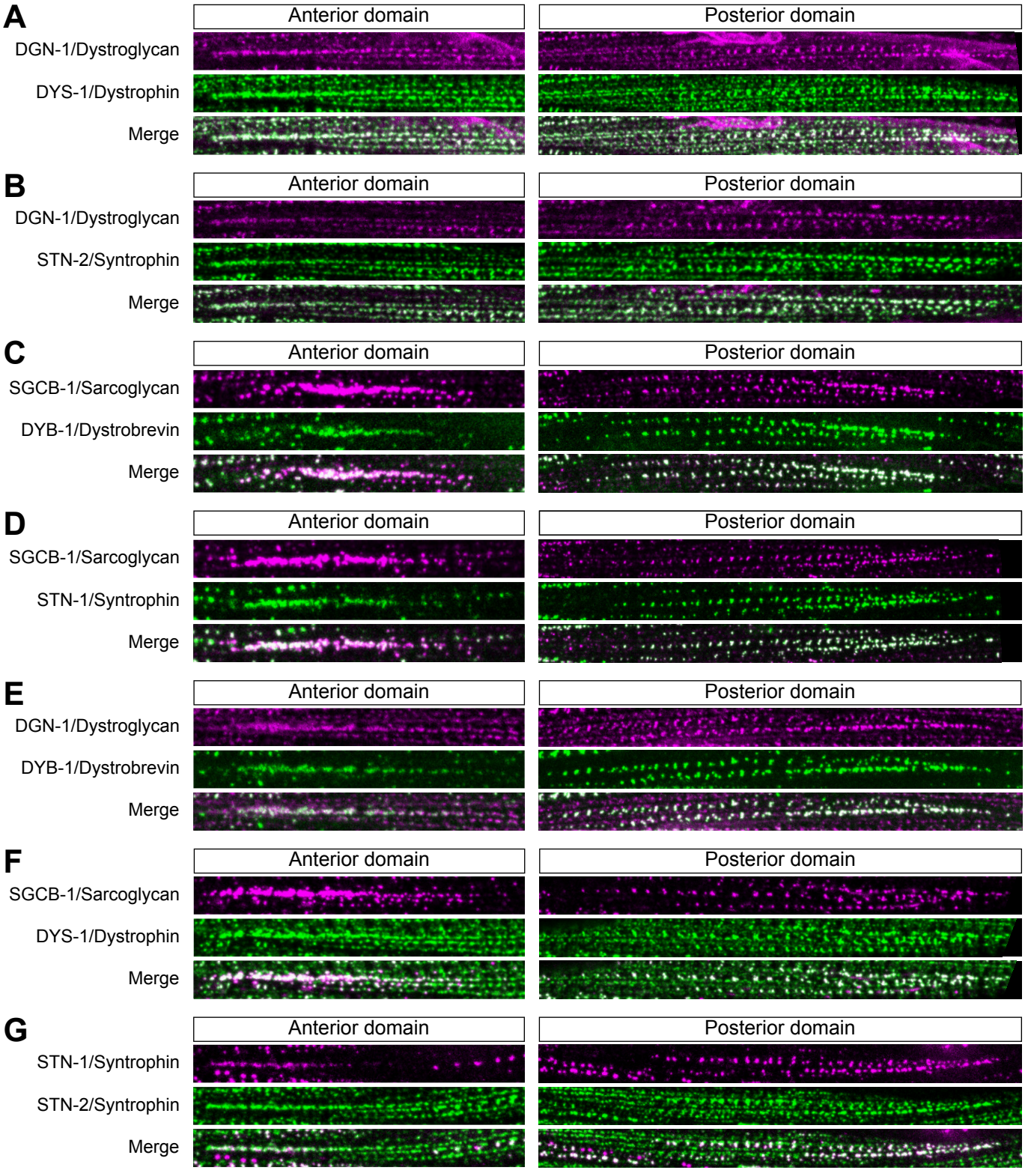
A
Anterior domain
Posterior domain
DGN-1/Dystroglycan
DYS-1/Dystrophin
Merge
B
Anterior domain
Posterior domain
DGN-1/Dystroglycan
STN-2/Syntrophin
Merge
C
Anterior domain
Posterior domain
SGCB-1/Sarcoglycan
DYB-1/Dystrobrevin
Merge
D
Anterior domain
Posterior domain
SGCB-1/Sarcoglycan
STN-1/Syntrophin
Merge
E
Anterior domain
Posterior domain
DGN-1/Dystroglycan
DYB-1/Dystrobrevin
Merge
F
Anterior domain
Posterior domain
SGCB-1/Sarcoglycan
DYS-1/Dystrophin
Merge
G
Anterior domain
Posterior domain
STN-1/Syntrophin
STN-2/Syntrophin
Merge

Figure S5

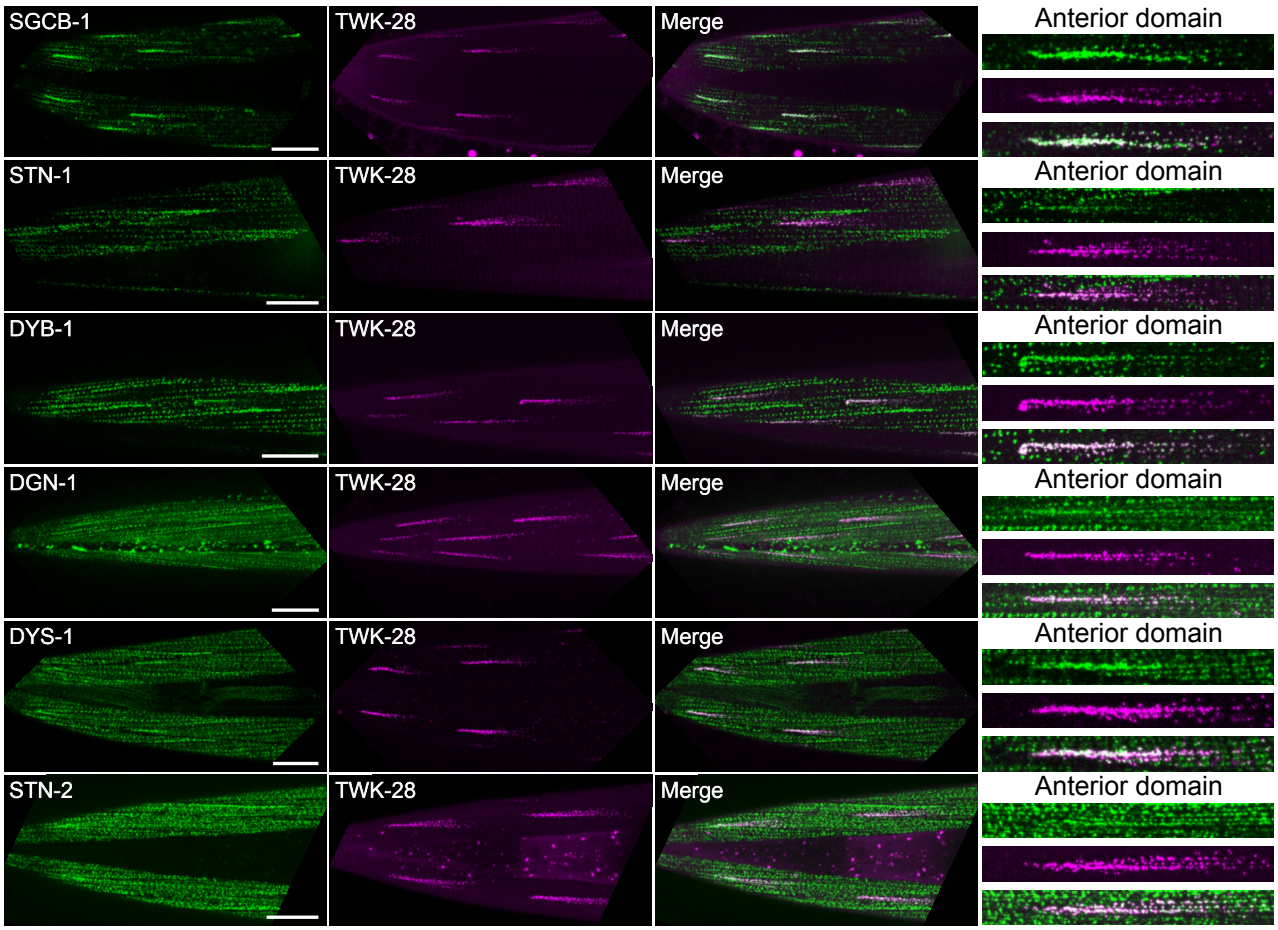

Figure S6

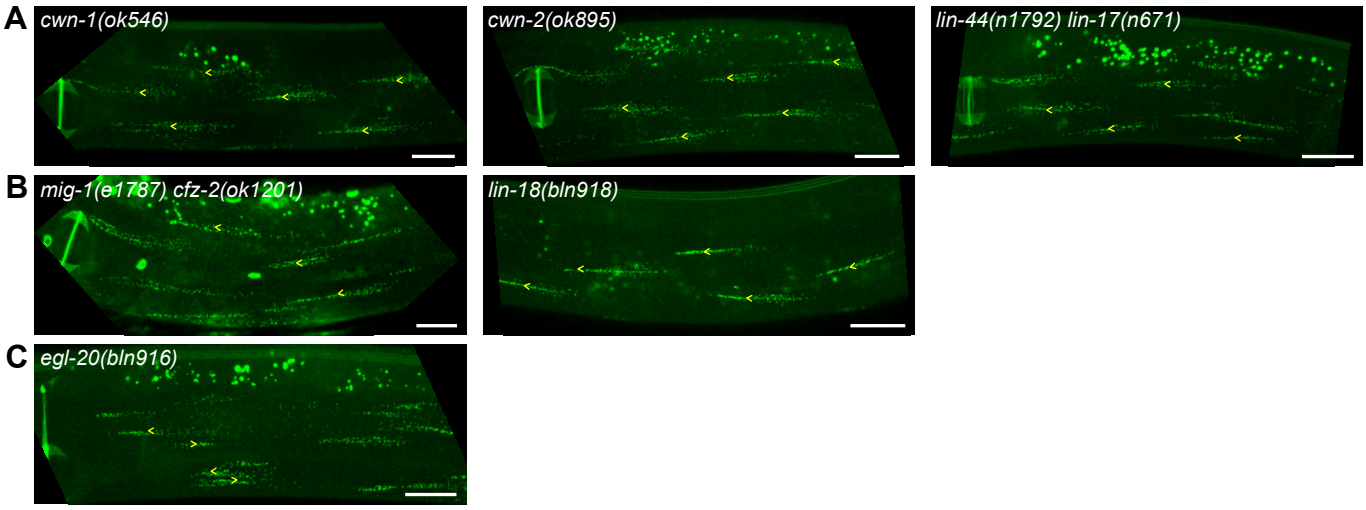
A
cwn-1(ok546)
cwn-2(ok895)
lin-44(n1792) lin-17(n671)
B
mig-1(e1787) cfz-2(ok1201)
lin-18(bln918)
C
egl-20(bln916)

Figure S7